Slip transition in dynamic wetting for a generalized Navier boundary condition

Valentin Rougier[a,b,*], Julien Cellier[a], Moussa Gomina[a], Joël Bréard[b,c,*]

[a] *CRISMAT, UMR 6508 CNRS, ENSICAEN, 6 Boulevard Maréchal Juin, 14050 Caen Cedex 4, France*
[b] *LOMC, UMR 6294 Université du Havre, 53 rue de Prony, 76058 Le Havre, France*
[c] *ABTE, Université de Caen, Bd Maréchal Juin, 14032 Caen, France*

Abstract

Hypothesis: Computer fluid dynamics simulations of dynamic wetting are often performed using a slip model on the substrate. In previous studies, the generalized Navier boundary condition (GNBC) has shown promising results and could help clear the gap between molecular and continuum scales, but lacks quantitative comparisons to experiments. We seek to investigate the dependence between the contact-line velocity and the slip length in a GNBC, by confronting numerical simulations to experimental data.

Experiments: The physical properties of a molten polymer (polyethylene glycol) were assessed thoroughly. Its dynamic contact angle on a cellulosic substrate was measured carefully using the Wilhelmy method. The experiment was reproduced in a finite elements model using a GNBC. It was repeated for capillary numbers between 10^{-6} and 10^{-1}, and slip lengths ranging from 1 µm to 1 mm.

Findings: A realistic value of the slip length was selected by matching the dynamic contact angles issued from numerical simulations and their exper-

*Corresponding author
Email addresses: valentin.rougier@ensicaen.fr (Valentin Rougier), joel.breard@unicaen.fr (Joël Bréard)

imental counterparts. The slip length behavior as a function of contact line velocity displayed a clear transition. The model also reproduced a dynamic wetting transition between frictional and viscous dissipations, which seems to be linked to an increasing difference between microscopic and macroscopic contact angles.

Keywords: Dynamic wetting, transition, slip length, generalized Navier boundary condition, polymer

---

1. Introduction

The modeling of multiphase flow is still an active research problem. In particular, wetting dynamics, which deals with time evolution of moving contact lines on solid surfaces, also plays a role in a variety of natural phenomena, from groundwater flows to the famous example of water striders. It is also present in a number of industrial applications such as oil recovery, polymer processing, paint coating, composites manufacturing and many more.

The current study was developed in the context of liquid composite molding (LCM) processes for composites manufacturing. This family of processes involves phenomena occurring at different scales, and in particular capillary phenomena represent the smallest scale that is usually considered by studies. The void content, which should be minimized to improve the mechanical properties of a part, is influenced by the interplay between capillarity and viscosity. The evolution of voids is also heavily dependent on the velocity of liquid-gas interfaces [1, 66]. The role of capillarity was nevertheless ignored for a long time, and is still being neglected in many applications where production rate is preferred, engendering defective parts. In this context dy-

namic wetting is also of particular interest, since the quality of fiber-matrix adhesion is known to depend on fiber wettability [17].

Considering those facts, we will focus on a liquid displacing a gas on a solid surface, idealized as a smooth and rigid phase. This case, while simplified by the absence of defects when compared to real surfaces [3, 4], still encompasses multiple challenges. First, we will briefly present some theoretical models tackling this situation, as well as numerical approaches developed to simulate a moving contact line. Next, we will use numerical simulations to model the problem, the results of which will be compared with experimental data. It turns out that this procedure reveals various transitions and mechanisms, some of which may be linked to the numerical model, and others presumably to more fundamental mechanisms.

2. Modeling multiphase flow

Even though the first pioneer models in wetting dynamics were formulated more than 50 years ago, the variety of phenomena involved makes the establishment of a complete theory a formidable task. The extreme care needed in experimental characterization of dynamic wetting and the difficulty to reproduce ideal systems makes this even more difficult. This might explain why, to this date, even a model dealing with the ideal case of a smooth solid, a simple Newtonian liquid and an inviscid gas, is yet to be established and accepted by the scientific community. The already existing models can generally be grouped by families, according to the framework in which they were established [13, 22, 36, 59]. They usually give a relationship between the macroscopic dynamic contact angle θ, which is the angle obtained by direct experimental measurements, and the contact-line velocity

V. The latter is generally represented by the dimensionless capillary number $\mathrm{Ca} = \eta V/\sigma$, where σ is the liquid-gas surface tension and η is the dynamic viscosity of the liquid.

2.1. Theoretical models

Some of the earlier models involve statistical physics and deal with molecular displacements at the contact line. The molecular kinetic theory (MKT), initially proposed by Blake and Haynes in 1969 [10], was revisited and refined later to include different sources of free energy (viscosity [5] and adhesion [8]). These models generally express the contact angle as:

$$\cos\theta = \cos\theta_e - \Lambda \sinh^{-1}\left(\frac{\mathrm{Ca}}{\mathrm{C_B}}\right) \tag{1}$$

where θ_e is the equilibrium contact angle as defined by Young's law, $\Lambda = 2k_\mathrm{B}T/(\sigma\lambda^2)$ is a dimensionless thermocapillary ratio, λ is the average distance between reaction sites on the substrate for the adsorption of liquid molecules, T the temperature and k_B the Boltzmann constant. $\mathrm{C_B}$ was nicknamed the "Blake constant" by Petrov et al. [45], and depends on the flavor of MKT that is being used. In its second development, which takes the fluid viscosity into account, $\mathrm{C_B} = 2h\kappa_s\lambda/(\sigma v_m)$ where κ_s is the frequency of molecular displacements, v_m is the molecular flow volume and h the Planck constant.

Another family of models describes the problem using continuum mechanics. The so-called hydrodynamic theories (HD) deal with a macroscopic flow, and usually split the flow domain into multiple scales, matching each solution to obtain a global picture and extract a relationship between the macroscopic contact angle θ and the contact-line velocity V. This process also requires to deal with a contact line paradox: the viscous stresses diverge

when approaching the contact line with the usual no-slip boundary condition [31]. Some of the most known models in this family were formulated by Voinov [64] and Cox [20], often approximated as the Cox-Voinov law:

$$\theta^3 = \theta_\mu^3 + 9\Gamma \mathrm{Ca} \tag{2}$$

Here $\Gamma = \ln(x_{\max}/x_{\min})$ is used to close the contact line paradox, where $x_{\max}$ and $x_{\min}$ are macroscopic and microscopic cut-off lengths. They are usually considered to be the lengths between which capillarity is significant, and taken as $x_{\max} = \ell_c$ where $\ell_c = \sqrt{\sigma/(\rho g)}$ is the capillary length, and $x_{\min} = a$ is the size of the liquid molecules, at which hydrodynamic laws are no longer valid. θ_μ is a microscopic contact angle, viewed as a boundary condition for the interface shape. Many authors tend to use the equilibrium contact angle θ_e instead, which is not necessarily correct, but often stems from a lack of experimental or theoretical data on the microscopic contact angle. In his original paper, Cox [20] postulates that θ_μ should also depend on contact-line velocity, but keeps it constant in his approach.

Other models combine the two previous views, and consider the roles of friction and viscous dissipation occurring simultaneously. In particular, Petrov and Petrov's model [45, 46] uses the Cox-Voinov law, in which they replace the constant microscopic contact angle θ_μ by a dynamic contact angle computed with the MKT:

$$\theta^3 = \left[\cos^{-1}\left(\cos\theta_e - \Lambda \sinh^{-1}\left(\frac{\mathrm{Ca}}{\mathrm{C_B}}\right)\right)\right]^3 + 9\Gamma \mathrm{Ca} \tag{3}$$

This model thus takes into account not only two dissipation channels, but also two scales of the wetting process. It has proven to be quite successful to fit different kinds of experimental data, but can yield a poor agreement

between the values of parameters involved and their physical meaning.

Another promising theory, sometimes called the interface formation model (IFM), was established by Y. Shikhmurzaev over more than a decade of various publications [11, 35, 38, 54–57, 61]. This model, formulated in the frame of hydrodynamics and non-equilibrium thermodynamics, states that wetting a solid with a moving liquid causes the creation and destruction of interfaces. In this context, an elementary volume of fluid moves between a liquid-solid and a liquid-fluid interface in a finite amount of time. This leads to the apparition of a surface tension gradient around the contact line as the surface tension varies continuously, because of a local change in density. A generalized Navier boundary condition (GNBC) is used to describe the fluid-solid boundary. The GNBC provides a regularization to the contact-line paradox by taking into account the added stress caused by a surface tension gradient around the triple line. When moving further away from the interface, it reduces to the classical Navier boundary condition. The IFM does not enforce the contact angle, which rather arises as a response to the overall flow from the model. Although some authors questioned its physical meaning [25] or practicality [58] (the model involves a large number of parameters), it was also implemented in numerical simulations [42, 60, 61] with promising results.

2.2. Numerical models

As a powerful predictive tool for testing models and predicting the behavior of complex systems, numerical simulation has been used extensively to describe a moving contact line. A variety of boundary conditions were tested in the literature, with different numerical methods and domains of validity.

Continuum CFD models, solving the Navier-Stokes equation in the fluid phases, represent a common way of treating interfaces. Allowing the description of a wide variety of scales in the flow, they are still by nature unable to reproduce microscopic phenomena, and need to include them as phenomenological constants or boundary conditions. They decompose the fluid domain as a grid, made of elementary cells or elements of variable sizes, over which the fields and variables are discretized and evaluated. An additional method is then used to discriminate the immiscible fluids in the computational domain.

Popular frameworks in CFD include the Volume of Fluid (VoF) approach, using the PLIC method to reconstruct the interface [70]. It can also handle interfaces [47] and contact lines [30] using penalty terms in the boundary conditions.

The Finite Elements Method (FEM), which is probably the most used in scientific computing, is a good candidate for multiphysics problems. This potential for coupling makes it an interesting framework to simulate moving contact lines, since they are often influenced by other phenomena such as heat transfer or substrate deformation. Interface tracking can be achieved by additional layers such as the level set method. It is an originally non-conservative approach, deducing the interface from a signed distance function, then advected by the velocity field. A conservative form was formulated afterwards [43, 44], improving the method's accuracy for the description of multiphase flow.

A boundary condition on the solid surface is then required for wetting. The simplest approach of imposing the contact angle to be its equilibrium value θ_e as a boundary condition works for static contact lines, but is non-

physical when they move [68]. Some different approaches include setting the dynamic contact angle from a theoretical model [27], using a Navier slip model, or imposing an exhaustive mechanical equilibrium that includes capillary effects [16, 19]. This last approach can be linked to the use of a generalized Navier boundary condition [51, 68, 69], which other studies found to adequately model dynamic wetting, but also introduces new parameters which, to the best of our knowledge, haven't been studied so far.

Sharp interface models are also commonly used for free-surface flows. In this case, an arbitrary Lagrangian-Eulerian (ALE) formulation in which the computational domain follows the deformations of the free surface is often preferred. While this method provides a more precise description of interfaces, it prevents topological changes, which could have been an interesting feature to investigate different mechanisms such as the apparition of bubbles. The GNBC [26] and the interface formation model [42, 61] were also implemented successfully in this framework.

Simulations at the microscopic scale are generally tackled with molecular dynamics (MD). Using classical interatomic potentials (usually Lennard-Jones potentials), simple systems such as droplets are left to evolve, and may then be described at a macroscopic scale with thermodynamic quantities by averaging procedures. While these models are supposed to yield significant results due to the use of relatively fundamental mechanisms, they are limited by the computing power that is required to run a simulation. The systems typically involve up to a million of particles, and evolve for a short amount of time (nanoseconds to microseconds) [2]. Multiphase flow can be modeled by MD simulations, for which each phase is given a possibly different potential. This allows to describe the evolution of a contact line, and thus study

dynamic wetting. Authors often rely on MD to explore nanometric scales for which no experimental observation is available yet.

MD is also a powerful pathway for upscaling, by comparing behaviors at the molecular and continuum scales. It was recently used to demonstrate how the inclusion of mass exchange across a wall can help regularize slip models [37]. MD studies confirmed the validity of MKT at microscopic scales for simple liquids [21], with Wang et al. suggesting that the modeling of both microscopic and macroscopic scales is needed when larger systems are being described [65].

In 2003, Qian et al. modeled the dynamics of immiscible two-phase Couette and Poiseuille flows using molecular dynamics [50]. They showed that the whole solid-liquid boundary follows the GNBC, and that a continuum hydrodynamics formulation of the same system with a GNBC yields similar results. This important result motivates the use of this boundary condition to describe the time evolution of a contact line.

3. Experimental data

An experimental study of polyethylene glycol (PEG) with molecular weights M_n = 1450 to 20 000 g/mol spreading on a cellulosic substrate was carried out (for more information on the substrates, see the supplementary material). The substrates were attached to a tensiometer, plunged at different constant velocities in the melted polymer with a controlled temperature, while the advancing contact angle was being measured by the Wilhelmy method.

The relevant properties of PEGs were also measured in the 75 to 120 °C range. This allowed the definition of material properties for surface ten-

ρ	η	σ	θ_e
$\mathrm{kg/m^3}$	$\mathrm{Pa \cdot s}$	mN/m	rad
1088	0.16	41.1	0.88

Table 1: Relevant material properties of the PEG 3350 used in this study, for a temperature of 75 °C.

λ	κ_s	Γ	χ^2
nm	GHz		
1.8 ± 0.1	13 ± 7	13.9	0.0009

Table 2: Parameters for the best fit to experimental PEG 3350 data by Petrov and Petrov's model. The molecular flow volume was computed as $v_m = M_n/(\rho N_\mathrm{A})$.

sion $\sigma(T)$, density $\rho(T)$, and viscosity $\eta(T)$ in those particular conditions. For $M_n = 3500\,\mathrm{g/mol}$, surface tension and density were found to be linear functions of temperature with $\sigma = 47.14 - 0.08T$ mN/m and $\rho = 1148.0 - 0.8T$ $\mathrm{kg/m^3}$, with T in Celsius. Viscosity followed an Arrhenius law $\eta = 1.14 \cdot 10^{-5} \exp(2.83 \cdot 10^4/(RT))$ $\mathrm{Pa \cdot s}$, where R is the gas constant and T is in Kelvin. The liquid was found to be Newtonian in the range of temperature and shear rates involved. The static contact angles $\theta_e(T)$ on a cellulosic substrate were also measured. In this paper, we will focus on modeling the behavior of a PEG with $M_n = 3350\,\mathrm{g/mol}$ (Table 1).

The contact angle versus capillary number data was fitted with different models. Petrov and Petrov's model was deemed the most accurate to interpolate the data, and the resulting parameters are given in Table 2 for the PEG 3350. They will be used later in this study to assess and check numerical simulations.

4. Numerical study setup

The numerical model aims at reproducing the experiments described in the previous section. The experimental data will then allow to assess, compare and correct the numerical results.

The experiment is modeled as a monolithic fluid flow and the problem is solved by the finite elements method with COMSOL Multiphysics®. A gas (air) and a liquid (PEG 3350) are distinguished by using a level set function Φ which tracks the liquid-gas interface. It is defined as a scalar function of the signed distance from the interface, and varies between 0 (gas) and 1 (liquid) within the domain.

Its implementation in COMSOL is initialized as a function of the distance from the interface d_0 in the whole domain as:

$$\Phi = \frac{1}{1 + e^{\pm d_0/\varepsilon}} \tag{4}$$

where ε represents the characteristic interfacial width. Φ can be seen as a smeared Heaviside function, allowing the computation of a smooth gradient.

The fluid density ρ and dynamic viscosity η then depend on the value of Φ, giving the two phases their properties that vary smoothly at the interface:

$$\begin{cases} \rho = \rho_g + (\rho_l - \rho_g)\Phi \\ \eta = \eta_g + (\eta_l - \eta_g)\Phi \end{cases} \tag{5}$$

The subscripts l and g represent the liquid and gas phases respectively.

The level set function is advected by a velocity field $\mathbf{u} = ue_x + ve_y$ and its evolution is governed by a convection-diffusion equation:

$$\frac{\partial \Phi}{\partial t} + \mathbf{u} \cdot \nabla \Phi = \gamma_{LS} \nabla \cdot \left[\varepsilon \nabla \Phi - \Phi(1 - \Phi) \frac{\nabla \Phi}{|\nabla \Phi|} \right] \tag{6}$$

Here γ_{LS} is a reinitialization parameter, controlling the amount of reinitialization of the level set function. Reinitialization steps are used to enforce the preservation of the signed distance function and to retain the regularity of Φ [18, 28, 40].

The fluid flow is governed by the Stokes equation for an incompressible liquid:

$$\begin{cases} \rho \dfrac{\partial \mathbf{u}}{\partial t} = \nabla \cdot \left[-p\mathbf{I} + \eta(\nabla \mathbf{u} + (\nabla \mathbf{u})^T) \right] + \rho \mathbf{g} + \mathbf{F}_{st} \\ \nabla \cdot \mathbf{u} = 0 \end{cases} \tag{7}$$

where p is the pressure, $\mathbf{g} = -ge_y$ is the acceleration of gravity, and $\mathbf{F_{st}}$ is a surface tension force which stems from the pressure jump at the curved interface according to Laplace's law. This surface tension force is evaluated by using the continuum surface force (CSF) method [15] as:

$$\mathbf{F_{st}} = \sigma \delta \kappa \mathbf{n} + \delta \nabla_s \sigma \tag{8}$$

where $\mathbf{n} = \nabla\Phi / |\nabla\Phi|$ is the unit vector normal to the interface, $\nabla_s = (\mathbf{I} - \mathbf{n}\mathbf{n}^T)\nabla$ is the gradient operator along the free surface, $\kappa = -\nabla \cdot \mathbf{n}$ is the local interface curvature and $\delta = 6|\nabla\Phi||\Phi(1-\Phi)|$ is a smoothed Dirac function centered on the diffuse interface.

The second term in Equation 8 represents a Marangoni-induced force which may originate from a temperature gradient along the interface, or another source of surface tension gradient. One can also relate it to Shikhmurzaev's interface formation model, which assumes that the surface tension varies continuously from its liquid-gas to its liquid-solid equilibrium value across the triple line. In his model however, this variation is supposed to mainly

stem from the global flow shearing the interface, which is not what happens in the present setup.

A consistent streamline and crosswind artificial diffusion scheme is used for stabilization. The level set and Stokes equations are solved on quadratic and P2/P1 elements respectively.

4.1. Geometry and boundary conditions

4.1.1. Geometry

The flow on one side of the Wilhelmy plate is reproduced (Figure 1). The flow occurring between the bottom of the vessel and the plate is considered negligible, and one takes advantage of the configuration to consider only one side of the plate. Then, neglecting the influence of the plate borders allows to use a 2D model. The surface of the substrate is represented by the left-hand side boundary. At the initial state, each of the two fluids occupies one half of the domain (top or bottom), and the air-liquid interface is horizontal – forming a 90° angle with the solid. More details on the choices motivating the dimensions of the model are given in the supporting material.

4.1.2. Generalized Navier boundary condition (GNBC)

As shown by the literature [31], setting the classical no-slip boundary condition on a liquid-solid boundary is not physically acceptable, since it results in a stress singularity at the contact line and prevents its displacement. A boundary condition allowing the fluid to slip on the wall is thus necessary. This means that the velocity of the wall and the tangent velocity in the liquid near the wall may differ. The difference between these velocities, called slip velocity v_{slip}, depends on the slip model applied on the boundary.

Various slip models have been studied to relieve the singularity caused by a no-slip condition. Among them, the classical Navier boundary condition

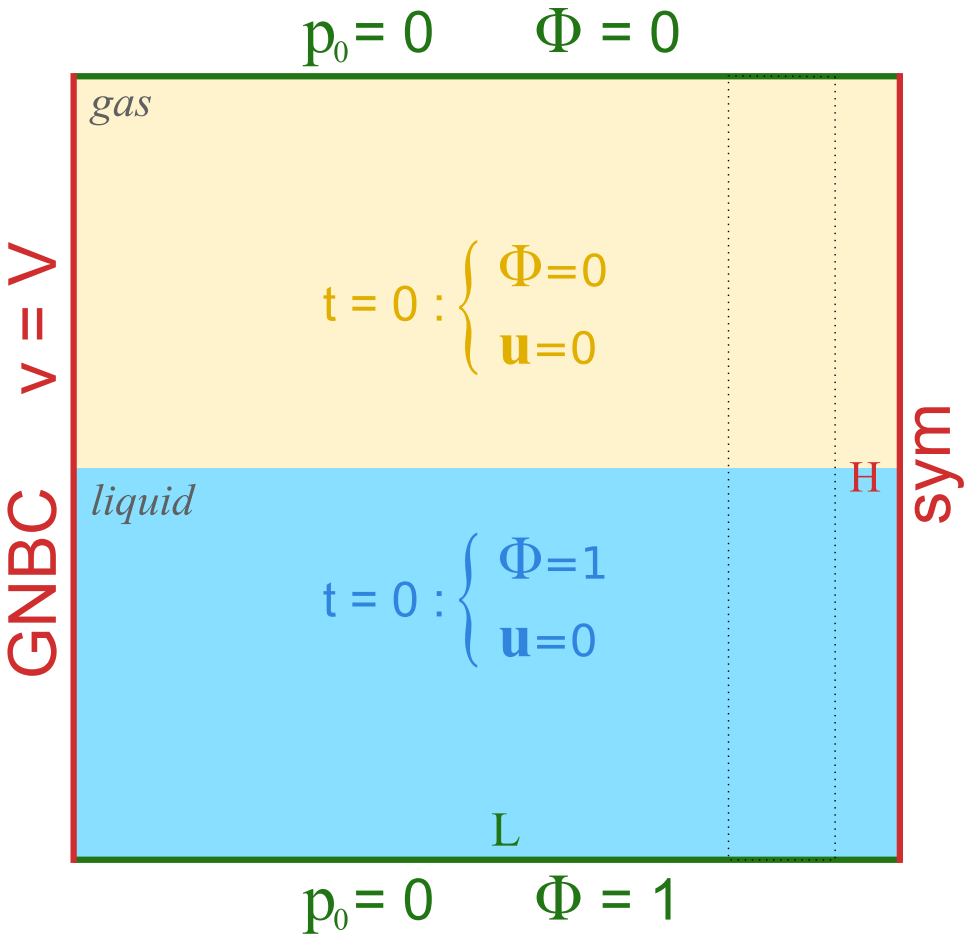

Figure 1: Geometry and boundary conditions of the Wilhelmy plate simulation at the initial state. The subdomain located between the dashed lines will be used later to compute a macroscopic contact angle.

(NBC) allows the liquid to slip on the solid surface, at a magnitude that is proportional to the exerted viscous stress. However, this approach requires the addition of an extra condition on the contact angle to close the problem for multiphase flow, making it system-dependent [14, 53]. Considering the lack of a globally accepted contact angle model, the Navier boundary condition is not retained in this work.

A generalization of the Navier boundary condition has already been proposed and used by various authors for the modeling of a moving contact line [12, 39, 49, 51, 53, 54, 57, 60, 68]. The GNBC states that the amount of slip on the solid boundary is proportional to the total stress level, including the viscous stress τ_{visc} like the NBC, but also the uncompensated (or unbalanced) Young's stress $\tau_{\text{Y}} = \sigma(\cos\theta - \cos\theta_e)$. This is necessary to correctly describe the presence of an interface because surface tension gives rise to this additional stress, and ultimately relieves the pressure singularity caused by viscous forces:

$$\frac{\eta}{\beta} v_{\text{slip}} = \tau_{\text{visc}} + \tau_{\text{Y}} \tag{9}$$

Here β represents a slip length, which may be interpreted as the extrapolated length inside the substrate for which the fluid velocity would vanish. The slip length controls the total amount of dissipation at the boundary, caused by solid-fluid friction. It is often expressed as a slip coefficient $\mathcal{B} = \eta/\beta$. The viscous stress in the y-direction can be decomposed into its normal and tangential contributions as $\tau_{\text{visc}} = \tau_{yy} + \tau_{yx}$.

Shikhmurzaev's interface formation model uses a similar condition to describe an *apparent* slip in the interfacial region. Slippage reflects a velocity difference between the solid and liquid layers facing the interface, induced

by a surface tension gradient. An important difference with the current model lies in the mechanism responsible for the fluid motion. The interface formation model implies that the unbalanced Young's force originates from a local variation of the surface tension around the triple line, which is primarily caused by the flow field. Applying Young's law, a dynamic value of the contact angle appears naturally. Here, the unbalanced Young's force stems from a deviation of the microscopic contact angle from its equilibrium value. The IFM could thus be seen as a more fundamental description of the sheared interfacial layer, with the present model only extracting the resulting apparent slip and uncompensated Young's stress as boundary conditions.

In the present model, the GNBC is applied on the solid boundary (Figure 2), and is expressed as:

$$\sigma\delta(\mathbf{n}\cdot\mathbf{n}_w - \cos\theta_e)\mathbf{n} + \tau_{\text{visc}} = -\frac{\eta}{\beta}(\mathbf{u}-\mathbf{U}) \tag{10}$$

Here $\mathbf{U}$ is the prescribed wall velocity, and $\mathbf{n}_w$ is a unit vector normal to the boundary. In this expression, the microscopic contact angle is evaluated as $\cos\theta_\mu = \mathbf{n}\cdot\mathbf{n}_w$, and allows the calculation of the unbalanced Young's stress represented by the first term. This stress component is localized around the interface via the δ function. Since the fluid is Newtonian, the viscous stress τ_{visc} is expressed as $2\eta\dot{\gamma}$, where $\dot{\gamma} = \frac{1}{2}(\nabla\mathbf{u} + (\nabla\mathbf{u})^T)$ is the shear rate.

A non-penetration condition $\mathbf{u}\cdot\mathbf{n}_w = 0$ is also enforced. This condition sets the horizontal component of velocity v to zero, simplifying the expression for the shear rate $\dot{\gamma}$ since $\partial_y u = 0$ on the boundary.

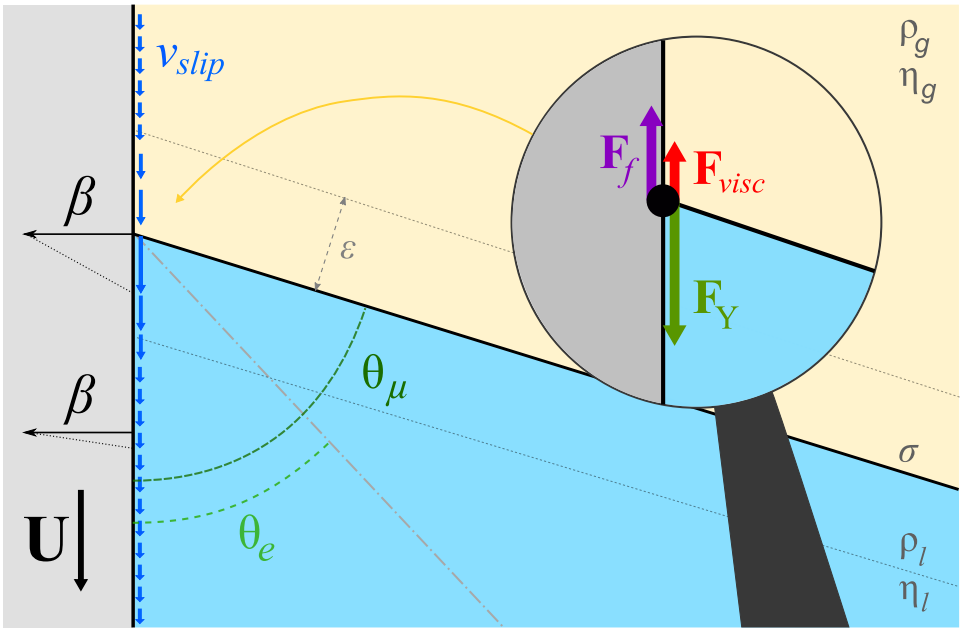

Figure 2: Diagram of the flow near a contact line according to the GNBC. An important slippage occurs on the solid boundary, and is reduced further away. The liquid-gas surface tension is constant, and the unbalanced Young force arises from a deviation of the microscopic contact angle. It is balanced by viscous drag and slippage-induced friction on the whole boundary.

4.1.3. Other boundary conditions and initial values

The level set function is set to $\Phi = 0$ and $\Phi = 1$ on the upper and lower boundaries respectively, forcing the presence of the gaseous and liquid phases. The pressure is imposed from a no tangential stress condition:

$$\mathbf{n}_w^T \left[-p\mathbf{I} + \eta \left(\nabla \mathbf{u} + (\nabla \mathbf{u})^{\mathbf{T}} \right) \right] \mathbf{n}_w = p_{\text{atm}} + \rho_l g h \tag{11}$$

Here $p_{\text{atm}} = 1$ bar is a constant atmospheric pressure. The boundary also enforces a normal flow via $\mathbf{u} \cdot \mathbf{t} = \mathbf{0}$ (where $\mathbf{t}$ is a tangential unit vector).

On the left-hand side boundary (representing the substrate), along with the GNBC, the boundary condition for the level set function is set to:

$$\begin{cases} \mathbf{n}_w \cdot \left[\varepsilon \nabla \Phi - \Phi(1-\Phi) \dfrac{\nabla \Phi}{|\nabla \Phi|} \right] = 0 \\ \mathbf{n}_w \cdot \mathbf{u} = 0 \end{cases} \tag{12}$$

4.2. Mesh and parameters

The geometry is discretized with a rather coarse structured mesh first, with elements of size $h_0 = 160\,\mu\text{m}$. A series of adaptive mesh refinements is then performed, in order to reach a final element size $h \leq 40\,\mu\text{m}$ in the areas of interest (details and illustration in the supplementary material).

The liquid properties are given in Table 1. Since this numerical study involves comparisons with experiments performed at 75 °C, this temperature will also be chosen for the current simulations. The air viscosity and density are set to $\eta = 0.021\,\text{mPa} \cdot \text{s}$ and $\rho = 1.014\,\text{kg/m}^3$. It should be noted that the effect of temperature on dynamic wetting has only been explored by a few researchers as of today [6, 48]. Since the current model takes the temperature dependence of material properties into account, it could be used as a basis for those studies. Another interesting feature of this model, the Marangoni effect described by the last term of Equation 8, is also known to

originate from temperature gradients along interfaces, and could be studied using this approach as well.

In a first approach, the slip length is set to be $\beta = h_0$. This parameter will be studied in more detail in section 5.

4.3. Dynamic contact angles

As the literature and our experiments point out, the measured value of a contact angle depends on the length scale at which it is evaluated. For a given situation, we will thus distinguish between a *macroscopic* contact angle θ and a *microscopic* contact angle θ_μ. The former can be measured directly by experiments, with length scales ranging from micrometers to the capillary length (a few millimeters). The latter is the angle formed by the liquid in the close vicinity of the solid at the molecular scale, which is usually nanometric. The microscopic contact angle is used as a boundary condition in hydrodynamic theories, which is also the case in the present study. It cannot be observed experimentally with conventional techniques, and therefore has to be computed from macroscopic data following a model. This brings the question of how the macroscopic and microscopic dynamic contact angles are being evaluated by the numerical model.

4.3.1. Macroscopic contact angles

Since the experimental data is measured using a tensiometer, a similar approach is chosen here: the macroscopic contact angles are derived from the total weight of the meniscus. This is achieved by measuring the difference between the mass of the liquid in the whole domain, and the mass of an equivalent system at rest with:

$$m = \int_\Omega \rho(\Phi)\, d\Omega - \frac{L}{L_0} \int_{\Omega_0} \rho(\Phi)\, d\Omega_0 \tag{13}$$

Here Ω_0 is a portion of the whole domain Ω in which the interface curvature is low. This subdomain of width $L_0 = 2\,\text{mm}$ can be spotted in Figure 1 (between the dashed lines) and in the mesh (see the supporting material). Since this is a 2D model, m has the dimension of a mass per unit length. The Wilhelmy equation is then used to compute the corresponding macroscopic contact angle:

$$\theta = \cos^{-1}\left(\frac{mg}{\sigma}\right) \tag{14}$$

4.3.2. Microscopic contact angles

A microscopic contact angle can also be evaluated numerically. The evaluation of this quantity is less straightforward, since in this model it is defined on the whole solid boundary (Equation 10), and may vary greatly away from the interface. It has no physical meaning outside of the contact line however, so its value will only be estimated near the center of the interface ($\Phi = 0.5$), by using the δ function. A weighted averaging across the whole boundary is then performed:

$$\cos\theta_\mu = \frac{\int_w (\mathbf{n}\cdot\mathbf{n}_w)\delta}{\int_w \delta} \tag{15}$$

Here w denotes the left-hand boundary (the solid-fluid interface), on which the GNBC is applied. The microscopic contact angle also depends on the wall velocity, and is given by the model according to the GNBC. Close to equilibrium, the microscopic and macroscopic contact angles take similar values. We will show in section 5 that for a specific set of conditions, this is no longer the case.

Yamamoto et al. suggested another approach that reduces the influence of the mesh resolution, which consists in computing the microscopic contact angle using the Cox-Voinov relation. This in turn would modify the evalu-

ation of the Young's force, but still requires the definition of a microscopic length, the selection of which still appears unclear.

4.4. Preliminary results

The simulation consists of a first step in which the meniscus evolves towards its equilibrium position for 2 seconds, by setting $\mathbf{U} = \mathbf{0}$. In a second step, starting from the previous near-equilibrium configuration, the plate velocity is imposed at a constant value $\mathbf{U} = -V\mathbf{e}_y$.

A first qualitative inspection yields satisfactory results. The meniscus height is dependent on the velocity at the boundary, and the dynamic contact angle varies monotonously from the equilibrium value. The flow in the liquid follows a rolling motion (Figure 3), which was observed experimentally by many authors [24, 52]. Similarly to previous studies [49, 51], it appears that the GNBC produces a large slip in the vicinity of the contact line, and retains the same characteristics as those found by previous studies.

A closer quantitative inspection is however needed in order to assess the physicality of these simulations. The resulting macroscopic contact angles can be compared to their experimental counterparts. While their velocity dependence are relatively similar, the values extracted from numerical simulations are smaller and the differences with experimental measurements increase when Ca is increased. We find indeed that modifying the slip length has a major influence on the contact angles. The wide range of values that can be displayed by the model for a given velocity is unphysical, since experiments yield a unique and repeatable value in each case. This cannot be ignored for further analyses: determining the slip length remains a topical issue. It is indeed the only parameter which may be tweaked easily, contrary to the interface width ε that would require refining the mesh.

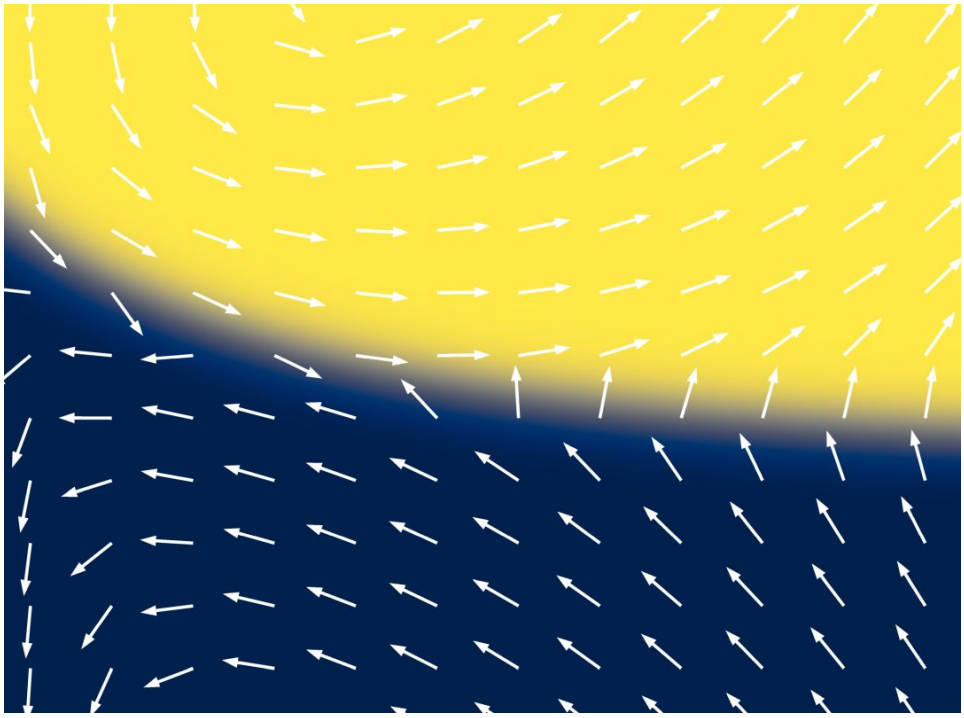

Figure 3: Zoomed-in view of the meniscus formed by PEG 3350 for a high wall velocity ($\mathrm{Ca} = 4.6{\cdot}10^{-3}$, $V = 70\,\mathrm{mm/min}$). The area shown here is approximately 7 mm by 4 mm. The velocity field shown here is not proportional.

5. Influence of the slip length

The slip length β expressed in the GNBC governs the amount of dissipation at the triple line. This friction mechanism, balancing the viscous and Young's stresses, provides a relation for the dynamic equilibrium of the contact line. The stresses depend on the overall flow profile, which influences the contact angle. This feature, which is well documented in the literature [7, 38, 67], is encouraging regarding the physicality of the GNBC. While the viscous stress is controlled by liquid properties, the Young's stress depends on surface parameters – usually lumped in the surface tension terms. The

slip length is then the only parameter that can modify the force balance, influencing the flow and thus modifying the contact angle.

5.1. Parametric study

To evaluate a realistic value for β, a series of parametric studies were performed. For a given liquid, starting from a meniscus at rest, the velocity of the solid boundary is imposed. The simulation is then run for 13 s, and β is varied as an exponentially decaying function of time from 10^{-3} to 10^{-6} m.

5.2. Force balance

Decreasing the slip length increases the macroscopic contact angle. The resulting increase in friction is balanced by the Young's and viscous stresses according to Equation 10 as shown in Figure 4b. The strong dependence between the microscopic contact angle and friction is shown in Figure 5b. For low velocities, the relation can be considered as linear. This indicates that in this regime, friction is mostly compensated by the deviation of the microscopic contact angle. At higher velocities, a different behavior appears, most probably caused by a large increase of viscous dissipation. This results in a transition discussed in subsection 5.3, where the two scales start to dissociate. Another consequence is that the velocity corresponding to the microscopic to viscous transition can be fine-tuned by the value of the slip length. A high amount of friction (corresponding to a small slip length) impedes the movement of the contact line.

This competition between frictional, viscous and Young's stresses is governed by the GNBC. It can be shown by the force balance in the y direction by integrating Equation 10 on the wall, in the vicinity of the liquid-gas

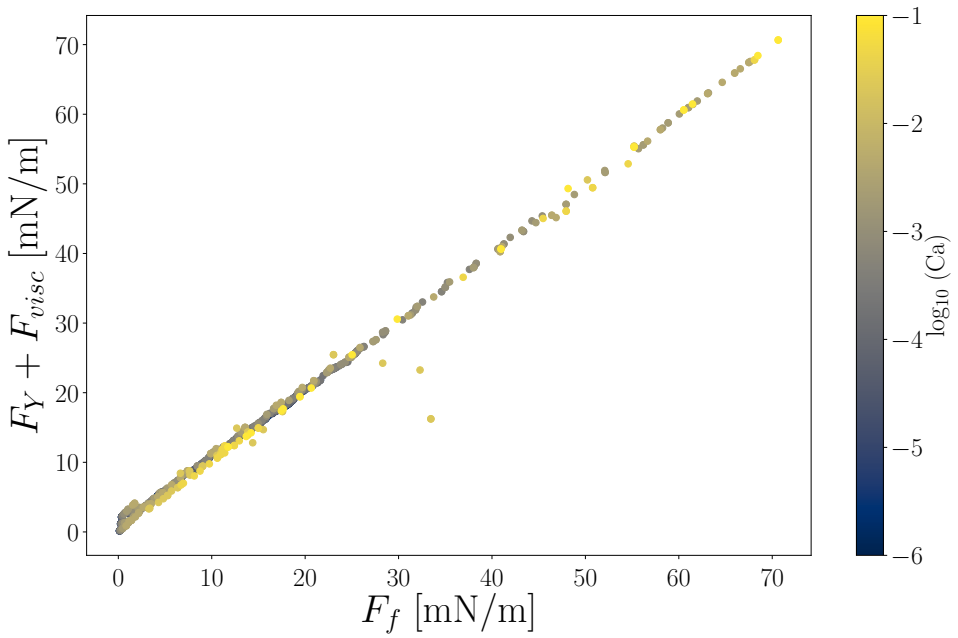

Figure 4: Sum of Young's and viscous forces plotted against the frictional force. Taking viscosity into account brings the high-velocity points back to the main curve compared to Figure 5b.

interface:

$$\sigma \int_w \delta(\cos\theta_\mu - \cos\theta_e)\, dw + \int_w \eta \left(2\frac{\partial v}{\partial y} + \frac{\partial v}{\partial x} + \frac{\partial u}{\partial x}\right) dw = -\frac{1}{\beta}\int_w \eta(v - V)\, dw \tag{16}$$

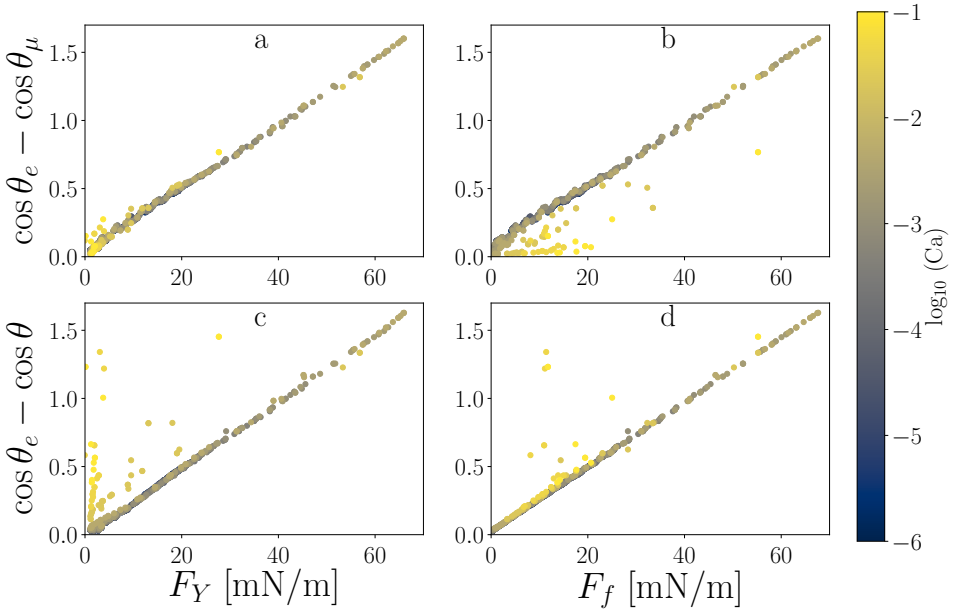

Figure 5: Deviation of the microscopic and macroscopic contact angle from the static value, plotted against friction and unbalanced Young's force. Each point corresponds to a different quasi-static situation controlled by the value of β. When comparing microscopic and macroscopic contributions, the microscopic origin of F_Y appears clearly, while the influence of viscous forces on the overall dissipation is also noticeable.

5.2.1. Uncompensated Young's force

Here, the uncompensated Young's force $F_Y = \sigma \int_w \delta(\cos\theta_\mu - \cos\theta_e)\, dw$ is viewed as a consequence of the microscopic dissipation. Consequently, the macroscopic contact angle is not a good indicator of the microscopic processes, and a discrepancy between F_Y and the force associated with

$\cos\theta - \cos\theta_e$ starts to appear at higher velocities (Figure 5 a and c). Since the GNBC takes the viscous forces into account unlike the Navier boundary condition, this difference is justified. It enables the evaluation of a velocity for which the microscopic dissipation no longer dominates, and for which viscous forces can no longer be neglected.

5.2.2. Viscous force

The viscous term is simplified by assuming that u vanishes on the boundary (no-penetration BC). This is verified in the simulation results. The viscous stress is however still difficult to predict because of its dependence on the velocity field, closely related to the contact angle itself. We can notice indeed that for values around $\theta = 90°$, the tangential component of the viscous stress τ_{yx} becomes small (Figure 6).

Without a model for the viscous stress exerted on a wall by an interface, it is not possible to predict the macroscopic contact angle that will be yielded by the GNBC, especially for the highest contact line velocities. Shikhmurzaev suggests using the solution given by Moffatt [41] for a flow in a corner.

5.2.3. Frictional force

In most cases, the viscous component is negligible in the vicinity of the contact line (Figure 5), where the Young's stress dominates by an order of magnitude. Assuming the microscopic contact angle is constant in the whole contact line area, Equation 10 could be approximated by a simpler form, yielding an analytic expression for the microscopic contact angle such that $\cos\theta_\mu = \cos\theta_e - \frac{\mathrm{Ca}}{\delta\beta}$. However, we face another issue in this case. The capillary number used here is derived from the wall velocity V, which is the

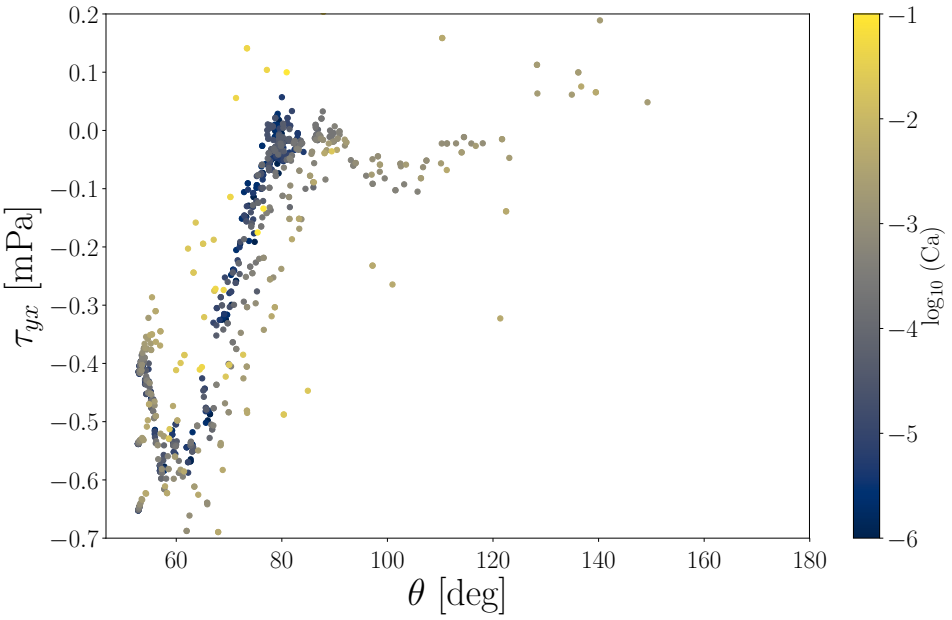

Figure 6: Dependence of the tangential component of the viscous stress on the macroscopic contact angle.

only one that is known. Computing the actual force balance would involve using the slip velocity $v - V$ at the wall instead. This quantity is however *a priori* unknown and is part of the solution to the weak problem. Estimations in the numerical simulations indicate an important difference between the slip velocity and the wall velocity, which makes this approach unsuitable.

This is where theoretical models could probably provide some additional information, because they provide a more fundamental explanation on the origin of slippage. The IFM describes how the apparent slip constitutes the response of the interface to an external constraint, generally imposed by the flow (an intuitive and more detailed explanation can be found in [11]). The MKT links the slip velocity to molecular processes at the triple line, and can yield a relation between the slip length and the local shear rate [9].

5.3. Dynamic wetting regime transition

When dissipation increases (high velocities and small slip lengths), the microscopic and macroscopic contact angles diverge rapidly with a sharp transition point. Their difference remains small for low contact line velocities and large slip lengths.

The threshold of very rapid growth of $\theta - \theta_\mu$ seems to originate from the apparition of viscous bending. As presented in subsection 5.2, when the velocity increases, the viscous stresses become significant in the overall dissipation. The microscopic contact angle θ_μ and the Young's stress increase slowly, and the morphology of the bulk flow is mostly influenced by viscous bending. The macroscopic contact angle θ then starts to increase rapidly, in agreement with the experimental data.

When fitting the experimental data with the Petrov and Petrov model, one can distinguish between the microscopic and macroscopic contact angles

by separating the MKT and HD contributions. In previous studies, this model was being fitted by letting Γ, λ, κ_s as free parameters. While the agreement between the model and data is generally excellent, the values obtained for the best fits tend to display unexpected values. This behavior is also observed with the Cox-Voinov model, for which unphysically high values of Γ are routinely found. If Petrov and Petrov's model is appropriate, we observe that the respective contributions of microscopic and macroscopic dissipations can take multiple values that would fit the data well. Meanwhile, for a given set of experimental conditions and a resulting contact angle, those contributions are uniquely defined. Since the microscopic dissipation is hardly measurable, an estimation of the viscous term is needed in order to find a unique solution.

Knowing this, following the approach of de Gennes [23], we set a fixed value of Γ by using the capillary length $\ell_c = \sqrt{\sigma/(\rho g)}$ for the macroscopic cut-off length, and the molecular size computed as $a = (\mathrm{M}_n/(\rho N_\mathrm{A}))^{1/3}$ for the microscopic cut-off, where N_A is the Avogadro constant. This value is then used for a fit of Petrov and Petrov's model, letting only λ and κ_s as adjustable parameters. The best fits for each liquid yield values of $\kappa_s = 13\,\mathrm{GHz}$ and $\lambda = 1.8\,\mathrm{nm}$ (Table 2). Those are acceptable values regarding their physical interpretation, as given by the MKT in Equation 1: they respectively represent an average of the molecular movements' frequency and distance.

Starting from the data for macroscopic contact angle θ fitted by the Petrov-Petrov model, the contribution of θ_μ can be extracted from Equation 3 as the first term of the right-hand side. While most models of dynamic wetting do not distinguish between these scales, this approach also allows to compute how the microscopic and macroscopic contact angles deviate

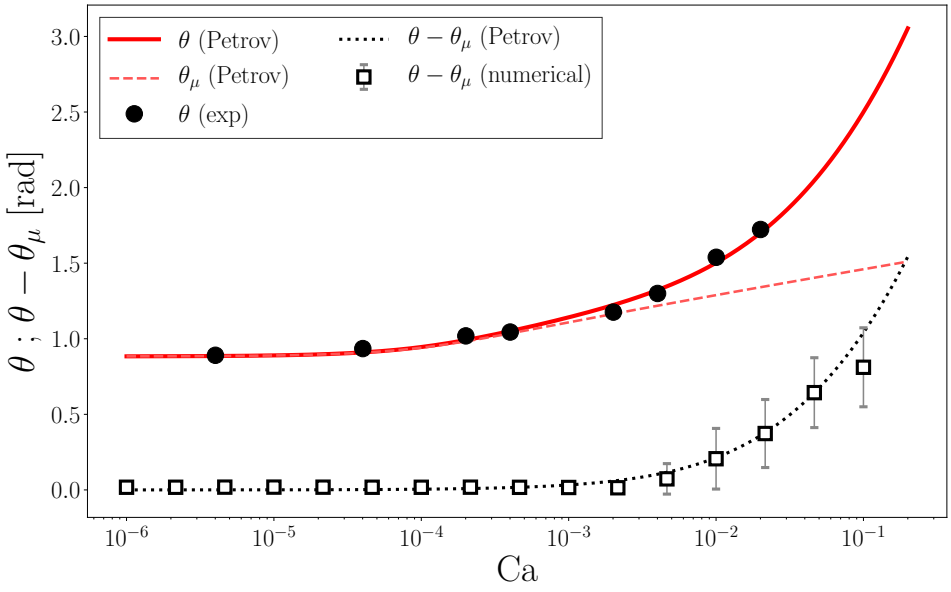

Figure 7: Petrov and Petrov fit on experimental data (full circles) for PEG 3350. The best values for this fit were $\lambda = 1.8\,\text{nm}$, $\kappa = 13\,\text{GHz}$. Γ was fixed to 13.9 by taking the capillary length and molecular size of PEG 3350. The macroscopic (full line) and microscopic (dashed line) contributions are represented, as well as their difference $\theta - \theta_\mu$ (dotted line). The latter starts to diverge around $\text{Ca} \approx 10^{-3}$. The same divergence is observed in the numerical simulations (empty squares), for which contact angles were averaged over 77 different slip lengths.

depending on the contact line velocity (Figure 7). The contribution of θ_μ keeps a relatively low value even at high Ca. The macroscopic contact angle stays very similar to θ_μ up to $\text{Ca} \approx 10^{-3}$. Then at higher velocities, viscous bending comes into play, and θ and θ_μ start to diverge.

This mechanism is well reproduced by the numerical simulations. Averaging $\theta - \theta_\mu$ over each slip length, it can be plotted for different contact-line velocities, and turns out to agree well with the best fit of Petrov and Petrov's model on experimental data. The viscous origin of this transition can be

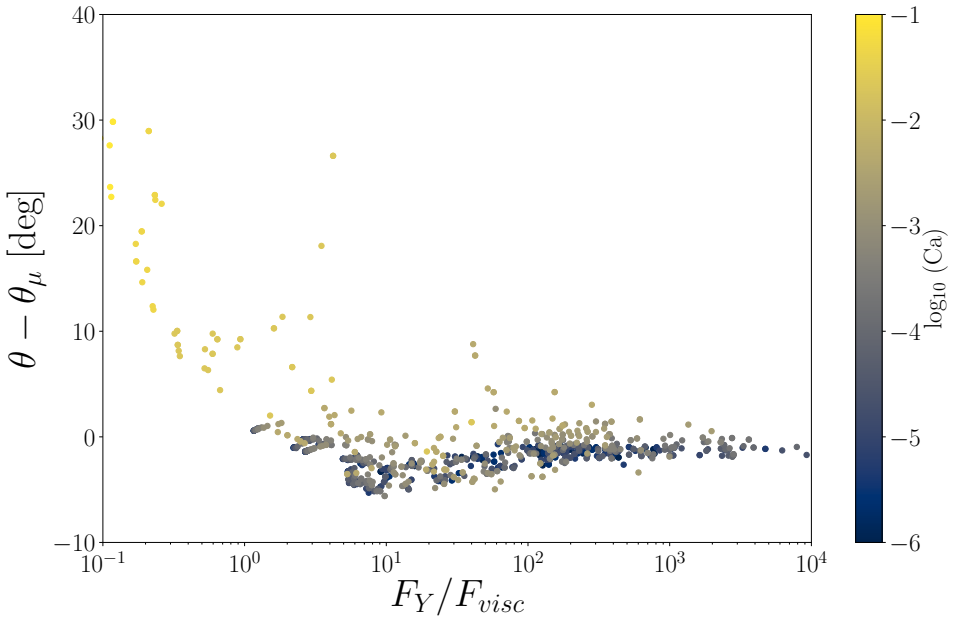

Figure 8: Evidence of the transition's viscous origin: the difference between the macroscopic and the microscopic contact angles is plotted against the ratio of the Young's force F_{Y} and viscous force F_{visc}. A transition occurs when $F_{\mathrm{Y}} \approx 10 F_{\mathrm{visc}}$.

shown by studying how the two scales separate. When the Young's force is dominant, θ_μ and θ are similar. Once the viscous force exerted in the contact line area reaches the same order of magnitude as the Young's force, the microscopic and macroscopic contact angles start to dissociate (Figure 8), and viscosity dominates the deformation of the free surface.

This interpretation can be linked to a recent study showing a very sudden appearance of viscous behavior in dynamic wetting [71]. The two domains are well described either by the MKT (low viscosities) or HD theories (high viscosities). Petrov and Petrov's approach constitutes an interesting combination of the two. Other studies started to show a divergence between the microscopic and macroscopic contact angles caused by an increase in contact

line velocity [33, 34]. While the scale dependence of contact angles is widely accepted, these two studies are, to the best of our knowledge, the only ones showing the influence of velocity on the separation between microscopic and macroscopic contact angles. The curves showing the velocity dependence are relatively similar to the present work and involve polymers as liquids or coating on the substrates, but were obtained using a different analysis. Interestingly, the critical capillary number at which the transition occurs was already identified in [33], but also in different contexts. The minimization of void content in LCM processes was indeed reached for this particular condition [29], and being a phenomenon driven by the competition between viscous and capillary forces, the overall picture seems consistent.

5.4. Velocity-dependence

The parametric study described in subsection 5.1 was performed for a range of plate velocities. This also allows to assess how the slip length β evolves with Ca in the present framework. Different θ versus β curves are obtained for each velocity. A velocity-dependent slip length was already observed and modeled for solid-liquid interfaces [32, 62, 63], and could thus constitute a reasonable hypothesis for a slip model applied to a moving contact line.

A realistic value of the slip length may then be selected by comparing the simulation results to experimental data. For a given plate velocity, the fit according to Petrov and Petrov's model θ_{fit} of the experimentally measured macroscopic contact angles is used to interpolate the experimental data. This in turn allows to select a physically acceptable value of the slip length for any imposed plate velocity, denoted β_0, for which the model matches experiments. The value of β_0 is identified by a linear fit of numerical

contact angles θ close to θ_{fit} for the same plate velocity: we find β_0 such that $\theta(\beta_0) \simeq \theta_{\text{fit}}$.

Using this procedure, a value of β_0 is then extracted for each value of Ca. The evolution of β_0 may then be plotted against contact line velocity (Figure 9). In the resulting curve, the slip length decreases exponentially until the system reaches a critical capillary number Ca_c, corresponding to a macroscopic contact angle $\theta = \pi/2$. The slip length then increases strongly when the velocity is increased, apparently following a power law. Overall, an empirical fit over each domain yields a velocity-dependence for β_0 such that:

$$\begin{cases} \text{Ca} < \text{Ca}_c : & \ln \beta_0 = \dfrac{-1}{a_1 \text{Ca} + b_1} \\ \text{Ca} > \text{Ca}_c : & \beta_0 = a_2 \text{Ca}^{3/2} + b_2 \end{cases} \tag{17}$$

Such a fit would yield $a_1 = 4.7{\cdot}10^{-6}$, $b_1 = 7.9{\cdot}10^{-2}$ and $a_2 = 1.7{\cdot}10^{-3}$, $b_2 = 5.6{\cdot}10^{-7}$. It was not plotted here due to the lack of a satisfying interpretation for those values, but some observations can still be made.

The transition displayed by β_0 as a function of contact-line velocity could stem from the increasing importance of viscous forces, which come with the augmentation of the capillary number. At low contact line velocities, the viscous stresses in the interfacial area are negligible compared to the Young's stress. The frictional dissipation is dominated by the slight increase of the microscopic contact angle, as stated by the GNBC. This either means increasing the slip velocity, or decreasing the slip length. Once the contact line velocity becomes important, an increase in the slip length moderates the increase in frictional dissipation. This means that in the interfacial area, the Young's stress can still be a dominant mechanism, without becoming

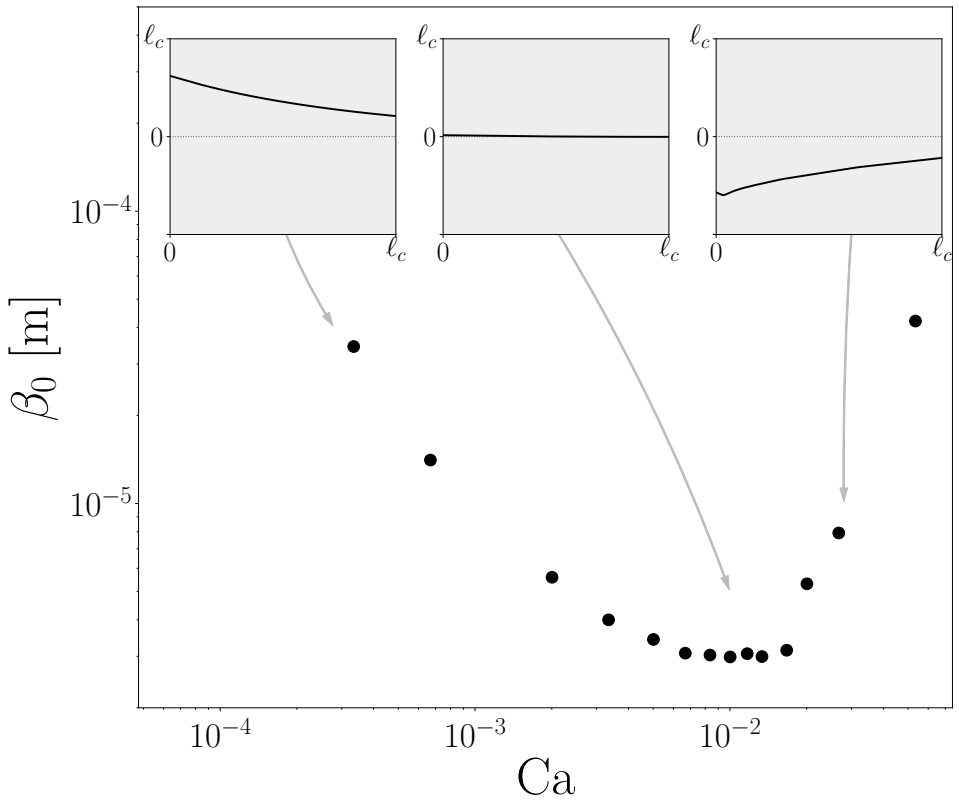

Figure 9: Velocity dependence of the slip length, as identified from the numerical and experimental data. Some close-ups of the corresponding interfaces are plotted in the insets for three regimes.

negligible compared to the viscous stress.

This transition could also be interpreted as a shift from a partially wetting to a non-wetting system, because here the sharp change in the slip behavior identified from the experiments corresponds to a contact angle $\theta = \pi/2$. In non-wetting conditions, dewetting becomes an energetically favorable mechanism. In our case, increasing the dynamic contact angle reduces the total solid-liquid interactions, and thus diminishes the total (frictional) dissipation. According to the GNBC, this can be achieved by increasing the slip length, which is what is observed in our results.

6. Conclusion

The dynamic equilibrium of a contact line was reproduced with the finite elements method using a diffuse interface model and a generalized Navier boundary condition (GNBC) on the solid interface. The simulations aimed at reproducing experimental data both qualitatively and quantitatively, to assess the evolution of a correct slip length β_0 in the GNBC. An experimentally observed transition between microscopic and macroscopic (viscous) dissipation could be reproduced [34, 48, 59], and seems to occur at similar velocities. The generalization of the Navier boundary condition, which does not directly enforce any model for the dynamic contact angle, seems to capture all of the characteristics that are observed experimentally (velocity dependence, rolling motion), in accordance with previous studies [49, 51, 68, 69].

A quantitative evaluation showed that the slip length β_0 has to vary with the contact line velocity to reproduce the contact angles measured experimentally. In previous studies however, the GNBC was implemented using

a constant value for the slip length. This parameter, while being seemingly of purely numerical nature, also appears in Shikhmurzaev's interface formation model [57], which uses a GNBC as well. One could interpret it as a characteristic of how the interface responds to shearing. The variation of β_0 required to obtain realistic contact angles displays a sharp transition with the contact line velocity. This transition seems to be linked to a mitigation of the large increase in viscous forces in the interfacial area induced by the high contact line velocity. It can also be interpreted as a switch in wettability, which would modify the energetic landscape.

The role of viscosity in this problem should be studied further in future works. While the situation that was modeled here involved a gas (air) of very low viscosity compared to the liquid phase, using two fluids of closer viscosities could yield interesting results, and modify the role of viscous stresses in the overall dissipation. This could be analyzed by expanding Petrov and Petrov's model [46] using the original formulation by Cox [20], which takes the ratio of viscosities between the two phases into account. This could again be compared to numerical simulations, assessing the role of the viscosity ratio on β_0. Other aspects of the liquid properties should be explored as well. Most models in wetting dynamics deal with *simple* liquids, and thus do not take the morphology of polymers into account. Meanwhile, polymers represent a family of materials that are used in many industrial processes involving contact lines. For instance, the effect of varying the molecular weight on dynamic wetting is still not known to this day.

Finally, models in wetting dynamics that involve non-Newtonian liquids are at a very early stage. Most of them deal with particular situations such as droplets spreading, total wetting or particular rheological models [36]. Knowing the importance of the viscous stresses in interfacial flows

and the common use of non-Newtonian polymers, the development of a model suitable for any liquid rheology would constitute a major achievement for wetting dynamics. While the theoretical development of such a model appears to be a formidable task, the GNBC's consistency encourages the use of a numerical study which, by comparison with experimental data, would constitute a first approach.

Acknowledgements

The authors thank Dr Benoît Duchemin for his help and advice in the experimental implementation. They thank DEPESTELE and all the partners in the TRAMPLIN project, supported by Bpifrance (Decision 2015-PIAVE-10).

References

[1] Abdelwahed, M.A.B., Wielhorski, Y., Bizet, L., Bréard, J., 2014. Bubble formation and transport in T-junction for application to Liquid Composite Molding: Wetting effect. Journal of Composite Materials 48, 37–48. doi:10.1177/0021998312467553.

[2] Allen, M.P., 2004. Introduction to Molecular Dynamics Simulation. Number 23 in NIC Series, John von Neumann Institute for Computing, Jülich.

[3] Bico, J., Marzolin, C., Quéré, D., 1999. Pearl drops. EPL (Europhysics Letters) 47, 220. doi:10.1209/epl/i1999-00548-y.

[4] Bico, J., Thiele, U., Quéré, D., 2002. Wetting of textured surfaces.

Colloids and Surfaces A: Physicochemical and Engineering Aspects 206, 41–46. doi:10.1016/S0927-7757(02)00061-4.

[5] Blake, T.D., 1993. Dynamic Contact Angles and Wetting Kinetics, in: Wettability. taylor & francis ed.. John C. Berg. number 49 in Surfactant Science Series, pp. 251–309.

[6] Blake, T.D., Batts, G.N., 2019. The temperature-dependence of the dynamic contact angle. Journal of Colloid and Interface Science 553, 108–116. doi:10.1016/j.jcis.2019.06.006.

[7] Blake, T.D., Bracke, M., Shikhmurzaev, Y.D., 1999. Experimental evidence of nonlocal hydrodynamic influence on the dynamic contact angle. Physics of Fluids 11, 1995–2007. doi:10.1063/1.870063.

[8] Blake, T.D., De Coninck, J., 2002. The influence of solid–liquid interactions on dynamic wetting. Advances in Colloid and Interface Science 96, 21–36. doi:10.1016/S0001-8686(01)00073-2.

[9] Blake, T.D., Fernandez-Toledano, J.C., Doyen, G., De Coninck, J., 2015. Forced wetting and hydrodynamic assist. Physics of Fluids 27, 112101. doi:10.1063/1.4934703.

[10] Blake, T.D., Haynes, J.M., 1969. Kinetics of liquid-liquid displacement. Journal of Colloid and Interface Science 30, 421–423. doi:10.1016/0021-9797(69)90411-1.

[11] Blake, T.D., Shikhmurzaev, Y.D., 2002. Dynamic Wetting by Liquids of Different Viscosity. Journal of Colloid and Interface Science 253, 196–202. doi:10.1006/jcis.2002.8513.

[12] Boelens, A.M.P., de Pablo, J.J., 2018. Generalised Navier boundary condition for a volume of fluid approach using a finite-volume method. Physics of Fluids 31, 021203. doi:10.1063/1.5055036.

[13] Bonn, D., Eggers, J., Indekeu, J., Meunier, J., Rolley, E., 2009. Wetting and spreading. Reviews of modern physics 81, 739.

[14] Bothe, D., Prüss, J., 2015. On the Interface Formation Model for Dynamic Triple Lines. arXiv:1504.04758 [physics] arXiv:1504.04758.

[15] Brackbill, J.U., Kothe, D.B., Zemach, C., 1992. A continuum method for modeling surface tension. Journal of Computational Physics 100, 335–354. doi:10.1016/0021-9991(92)90240-Y.

[16] Bruchon, J., Liu, Y., Moulin, N., 2018. Finite element setting for fluid flow simulations with natural enforcement of the triple junction equilibrium. Computers & Fluids 171, 103–121. doi:10.1016/j.compfluid.2018.06.007.

[17] Chang, H.W., Smith, R.P., Li, S.K., Neumann, A.W., 1985. Wettability of Reinforcing Fibers, in: Ishida, H., Kumar, G. (Eds.), Molecular Characterization of Composite Interfaces. Springer Berlin Heidelberg, Berlin, Heidelberg. Polymer Science and Technology, pp. 413–421. doi:10.1007/978-3-662-29084-2_25.

[18] Cheng, L.T., Tsai, Y.H., 2008. Redistancing by flow of time dependent eikonal equation. Journal of Computational Physics 227, 4002–4017. doi:10.1016/j.jcp.2007.12.018.

[19] Chevalier, L., Bruchon, J., Moulin, N., Liotier, P.J., Drapier, S., 2018. Accounting for local capillary effects in two-phase flows with relaxed

surface tension formulation in enriched finite elements. Comptes Rendus Mécanique 346, 617–633. doi:10.1016/j.crme.2018.06.008.

[20] Cox, R.G., 1986. The dynamics of the spreading of liquids on a solid surface. Part 1. Viscous flow. Journal of Fluid Mechanics 168, 169–194. doi:10.1017/S0022112086000332.

[21] De Coninck, J., Blake, T., 2008. Wetting and Molecular Dynamics Simulations of Simple Liquids. Annual Review of Materials Research 38, 1–22. doi:10.1146/annurev.matsci.38.060407.130339.

[22] de Gennes, P.G., 1985. Wetting: Statics and dynamics. Reviews of Modern Physics 57, 827–863. doi:10.1103/RevModPhys.57.827.

[23] De Gennes, P.G., Brochard-Wyart, F., Quéré, D., 2015. Gouttes, Bulles, Perles et Ondes. Belin, Paris.

[24] Dussan V., E.B., Davis, S.H., 1974. On the motion of a fluid-fluid interface along a solid surface. Journal of Fluid Mechanics 65, 71–95. doi:10.1017/S0022112074001261.

[25] Eggers, J., Evans, R., 2004. Comment on "Dynamic wetting by liquids of different viscosity," by T.D. Blake and Y.D. Shikhmurzaev. Journal of Colloid and Interface Science 280, 537–538. doi:10.1016/j.jcis.2004.07.001.

[26] Gerbeau, J.F., Lelièvre, T., 2008. Generalized Navier Boundary Condition and Geometric Conservation Law for Surface Tension. Report.

[27] Göhl, J., Mark, A., Sasic, S., Edelvik, F., 2018. An immersed boundary based dynamic contact angle framework for handling complex surfaces

of mixed wettabilities. International Journal of Multiphase Flow 109, 164–177. doi:10.1016/j.ijmultiphaseflow.2018.08.001.

[28] Gomes, J., Faugeras, O., 1999. Reconciling Distance Functions and Level Sets. Technical Report RR-3666. INRIA.

[29] Gueroult, S., Lebel-Lavacry, A., Park, C.H., Bizet, L., Saouab, A., Bréard, J., 2014. Analytical modeling and in situ measurement of void formation in liquid composite molding processes. Advanced Composite Materials 23, 31–42. doi:10.1080/09243046.2013.862383.

[30] Guillaument, R., Vincent, S., Caltagirone, J.P., 2015. An original algorithm for VOF based method to handle wetting effect in multi-phase flow simulation. Mechanics Research Communications 63, 26–32. doi:10.1016/j.mechrescom.2014.11.002.

[31] Huh, C., Scriven, L.E., 1971. Hydrodynamic model of steady movement of a solid/liquid/fluid contact line. Journal of Colloid and Interface Science 35, 85–101. doi:10.1016/0021-9797(71)90188-3.

[32] Léger, L.L., 2002. Friction mechanisms and interfacial slip at fluid solid interfaces. Journal of Physics: Condensed Matter 15, S19–S29. doi:10.1088/0953-8984/15/1/303.

[33] Lhermerout, R., 2016. Mouillage de Surfaces Désordonnées à l'échelle Nanométrique. Ph.D. thesis. Université de recherche Paris Sciences et Lettres.

[34] Lhermerout, R., Davitt, K., 2019. Contact angle dynamics on pseudo-brushes: Effects of polymer chain length and wetting liquid. Colloids

and Surfaces A: Physicochemical and Engineering Aspects 566, 148–155. doi:10.1016/j.colsurfa.2019.01.006.

[35] Lindner-Silwester, T., Schneider, W., 2005. The moving contact line with weak viscosity effects – an application and evaluation of Shikhmurzaev's model. Acta Mechanica 176, 245–258. doi:10.1007/s00707-004-0091-4.

[36] Lu, G., Wang, X.D., Duan, Y.Y., 2016. A Critical Review of Dynamic Wetting by Complex Fluids: From Newtonian Fluids to Non-Newtonian Fluids and Nanofluids. Advances in Colloid and Interface Science 236, 43–62. doi:10.1016/j.cis.2016.07.004.

[37] Lukyanov, A.V., Pryer, T., 2017. Hydrodynamics of Moving Contact Lines: Macroscopic versus Microscopic. Langmuir 33, 8582–8590. doi:10.1021/acs.langmuir.7b02409.

[38] Lukyanov, A.V., Shikhmurzaev, Y.D., 2007. Effect of flow field and geometry on the dynamic contact angle. Physical Review E 75, 051604. doi:10.1103/PhysRevE.75.051604.

[39] Manservisi, S., Scardovelli, R., 2009. A variational approach to the contact angle dynamics of spreading droplets. Computers & Fluids 38, 406–424. doi:10.1016/j.compfluid.2008.05.001.

[40] Min, C., 2010. On reinitializing level set functions. Journal of Computational Physics 229, 2764–2772. doi:10.1016/j.jcp.2009.12.032.

[41] Moffatt, H.K., 1964. Viscous and resistive eddies near a sharp corner. Journal of Fluid Mechanics 18, 1–18. doi:10.1017/S0022112064000015.

[42] Monnier, J., Witomski, P., 2004. Analysis of a Local Hydrodynamic Model with Marangoni Effect. Journal of Scientific Computing 21, 369–403. doi:10.1007/s10915-004-4095-y.

[43] Olsson, E., Kreiss, G., 2005. A conservative level set method for two phase flow. Journal of Computational Physics 210, 225–246. doi:10.1016/j.jcp.2005.04.007.

[44] Olsson, E., Kreiss, G., Zahedi, S., 2007. A conservative level set method for two phase flow II. Journal of Computational Physics 225, 785–807. doi:10.1016/j.jcp.2006.12.027.

[45] Petrov, J.G., Ralston, J., Schneemilch, M., Hayes, R.A., 2003. Dynamics of Partial Wetting and Dewetting of an Amorphous Fluoropolymer by Pure Liquids. Langmuir 19, 2795–2801. doi:10.1021/la026692h.

[46] Petrov, P., Petrov, I., 1992. A combined molecular-hydrodynamic approach to wetting kinetics. Langmuir 8, 1762–1767. doi:10.1021/la00043a013.

[47] Pianet, G., Vincent, S., Leboi, J., Caltagirone, J.P., Anderhuber, M., 2010. Simulating compressible gas bubbles with a smooth volume tracking 1-Fluid method. International Journal of Multiphase Flow 36, 273–283. doi:10.1016/j.ijmultiphaseflow.2009.12.002.

[48] Pucci, M.F., Duchemin, B., Gomina, M., Bréard, J., 2018. Temperature effect on dynamic wetting of cellulosic substrates by molten polymers for composite processing. Composites Part A: Applied Science and Manufacturing 114, 307–315. doi:10.1016/j.compositesa.2018.08.031.

[49] Qian, T., Wang, X.P., Sheng, P., 2003a. Generalized Navier Boundary Condition for the Moving Contact Line. Communications in Mathematical Sciences 1, 333–341.

[50] Qian, T., Wang, X.P., Sheng, P., 2003b. Molecular scale contact line hydrodynamics of immiscible flows. Physical Review E 68, 016306. doi:10.1103/PhysRevE.68.016306.

[51] Ren, W., E, W., 2007. Boundary conditions for the moving contact line problem. Physics of Fluids 19, 022101. doi:10.1063/1.2646754.

[52] Schwartz, A.M., Rader, C.A., Huey, E., 1964. Resistance to Flow in Capillary Systems of Positive Contact Angle, in: Contact Angle, Wettability, and Adhesion. American Chemical Society. volume 43 of *Advances in Chemistry*, pp. 250–267. doi:10.1021/ba-1964-0043.ch017.

[53] Shang, X., Luo, Z., Gatapova, E.Y., Kabov, O.A., Bai, B., 2018. GNBC-based front-tracking method for the three-dimensional simulation of droplet motion on a solid surface. Computers & Fluids 172, 181–195. doi:10.1016/j.compfluid.2018.06.021.

[54] Shikhmurzaev, Y.D., 1993. The moving contact line on a smooth solid surface. International Journal of Multiphase Flow 19, 589–610. doi:10.1016/0301-9322(93)90090-H.

[55] Shikhmurzaev, Y.D., 1994. Mathematical modeling of wetting hydrodynamics. Fluid Dynamics Research 13, 45. doi:10.1016/0169-5983(94)90063-9.

[56] Shikhmurzaev, Y.D., 1996. Dynamic contact angles and flow in vicinity

of moving contact line. AIChE Journal 42, 601–612. doi:10.1002/aic.690420302.

[57] Shikhmurzaev, Y.D., 2007. Capillary Flows with Forming Interfaces. CRC Press.

[58] Sibley, D.N., Savva, N., Kalliadasis, S., 2012. Slip or not slip? A methodical examination of the interface formation model using two-dimensional droplet spreading on a horizontal planar substrate as a prototype system. Physics of Fluids 24, 082105. doi:10.1063/1.4742895.

[59] Snoeijer, J.H., Andreotti, B., 2013. Moving Contact Lines: Scales, Regimes, and Dynamical Transitions. Annual Review of Fluid Mechanics 45, 269–292. doi:10.1146/annurev-fluid-011212-140734.

[60] Sprittles, J.E., Shikhmurzaev, Y.D., 2011. Finite Element Framework for Describing Dynamic Wetting Phenomena. International Journal for Numerical Methods in Fluids 65, 372–382. doi:10.1002/fld.2187, arXiv:1009.1418.

[61] Sprittles, J.E., Shikhmurzaev, Y.D., 2013. Finite element simulation of dynamic wetting flows as an interface formation process. Journal of Computational Physics 233, 34–65. doi:10.1016/j.jcp.2012.07.018.

[62] Thalakkottor, J.J., Mohseni, K., 2016. Unified slip boundary condition for fluid flows. Physical Review E 94, 023113. doi:10.1103/PhysRevE.94.023113.

[63] Thompson, P.A., Troian, S.M., 1997. A general boundary condition for liquid flow at solid surfaces. Nature 389, 360–362. doi:10.1038/38686.

[64] Voinov, O.V., 1976. Hydrodynamics of wetting. Fluid Dynamics 11, 714–721. doi:10.1007/BF01012963.

[65] Wang, G.J., Damone, A., Benfenati, F., Poesio, P., Beretta, G.P., Hadjiconstantinou, N.G., 2019. Physics of nanoscale immiscible fluid displacement. Physical Review Fluids 4, 124203. doi:10.1103/PhysRevFluids.4.124203.

[66] Wielhorski, Y., Ben Abdelwahed, A., Arquis, E., Glockner, S., Bréard, J., 2014. Numerical simulation of bubble formation and transport in cross-flowing streams. The Journal of Computational Multiphase Flows 6, 299–312. doi:10.1260/1757-482X.6.3.299.

[67] Wilson, M.C.T., Summers, J.L., Shikhmurzaev, Y.D., Clarke, A., Blake, T.D., 2006. Nonlocal hydrodynamic influence on the dynamic contact angle: Slip models versus experiment. Physical Review E 73, 041606. doi:10.1103/PhysRevE.73.041606.

[68] Yamamoto, Y., Ito, T., Wakimoto, T., Katoh, K., 2013. Numerical simulations of spontaneous capillary rises with very low capillary numbers using a front-tracking method combined with generalized Navier boundary condition. International Journal of Multiphase Flow 51, 22–32. doi:10.1016/j.ijmultiphaseflow.2012.12.002.

[69] Yamamoto, Y., Tokieda, K., Wakimoto, T., Ito, T., Katoh, K., 2014. Modeling of the dynamic wetting behavior in a capillary tube considering the macroscopic–microscopic contact angle relation and generalized Navier boundary condition. International Journal of Multiphase Flow 59, 106–112. doi:10.1016/j.ijmultiphaseflow.2013.10.018.

[70] Youngs, D.L., 1982. Time-dependent multi-material flow with large fluid distortion. Numerical Methods for Fluid Dynamics .

[71] Zhang, P., Mohseni, K., 2019. Viscous drag force model for dynamic Wilhelmy plate experiments. Physical Review Fluids 4, 084004. doi:10.1103/PhysRevFluids.4.084004.

Slip transition in dynamic wetting for a generalized Navier boundary condition: supplementary information

892

Valentin Rougier[a,b,*], Julien Cellier[a], Moussa Gomina[a], Joël Bréard[b,c,*]

[a] *CRISMAT, UMR 6508 CNRS, ENSICAEN, 6 Boulevard Maréchal Juin, 14050 Caen Cedex 4, France*
[b] *LOMC, UMR 6294 Université du Havre, 53 rue de Prony, 76058 Le Havre, France*
[c] *ABTE, Université de Caen, Bd Maréchal Juin, 14032 Caen, France*

A. Experimental data

a. Liquid properties

The relevant physical properties of the polymer used in this study, a polyethylene glycol with a molecular weight $M_n = 3350\,\mathrm{g/mol}$, were carefully assessed. They were studied for temperatures ranging from $T = 75$ to $120\,^{\circ}\mathrm{C}$.

Viscosity η***.***

The polymer viscosity was measured using a Malvern Kinexus Pro cone-plate rheometer. Its dependence on shear rate was measured for fixed temperatures of 65, 80, 100, 120, 150 and $180\,^{\circ}\mathrm{C}$. The experimental data was fitted by a Carreau-Yasuda model for the dependence on shear rate $\dot{\gamma}$, and by an Arrhenius model for the dependence on temperature T:

$$\eta(\dot{\gamma}) = 0.122 + 0.024\left[1 + (\dot{\gamma}/161)^{1.57}\right]^{-1/1.57} \quad \mathrm{Pa\cdot s} \tag{A.1}$$

In the experimental conditions of the dynamic contact angles measurements, the PEG was considered to be in the Newtonian plateau, and could thus be treated as a Newtonian liquid. The shear rate in the contact line area resulting from the numerical simulations is plotted and compared to the liquid rheology in Figure I.

*Corresponding author
Email addresses: valentin.rougier@ensicaen.fr (Valentin Rougier), joel.breard@unicaen.fr (Joël Bréard)

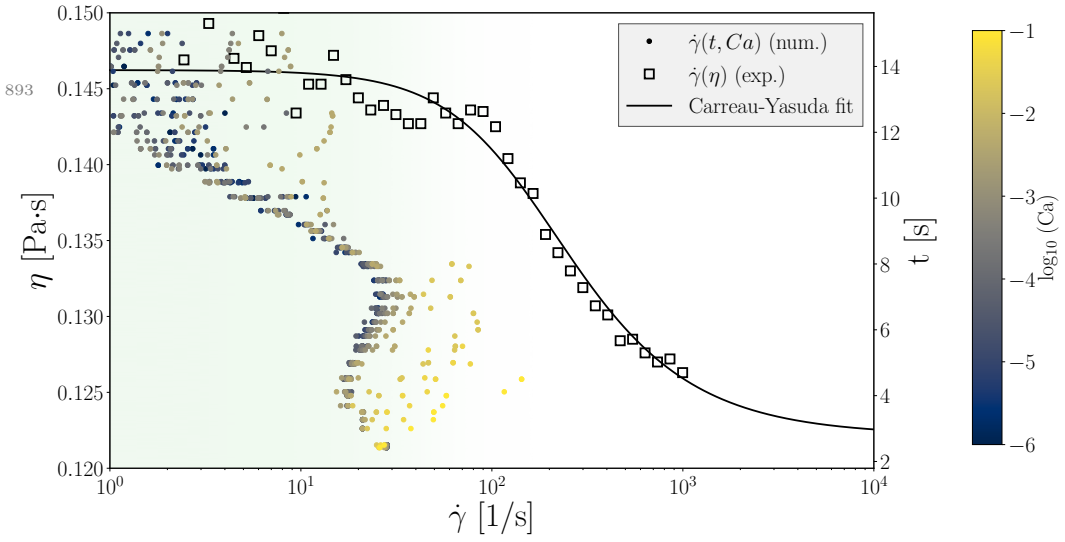

Figure I: Evolution of PEG3350 viscosity with the shear rate, compared with the numerical estimations of shear rate in the contact line area.

The dependence on temperature T was measured at a fixed shear rate of $100\,\mathrm{s}^{-1}$. The temperature was increased from 60 to 200 °C with a rate of $1\,°\mathrm{C}\cdot\mathrm{min}^{-1}$, and the data was fitted by an Arrhenius model:

$$\eta(T) = 1.14 \cdot 10^{-5} \exp\left(\frac{2.83 \cdot 10^4}{RT}\right) \quad \mathrm{Pa}\cdot\mathrm{s} \tag{A.2}$$

where R is the gas constant, and T is the temperature in Kelvin. A good correspondance was found with the data yielded by the study of shear rate (Figure II).

Density ρ**.**

The density was measured with a Dataphysics DCAT25 microbalance, equipped with a calibrated density probe. For each temperature, 3 measurements of buoyancy were averaged, and the temperature-dependence of density could be fitted by a linear relation (Figure III):

$$\rho(T) = 1148.0 - 0.8T \quad \mathrm{kg/m}^3 \tag{A.3}$$

where T is the temperature in Celsius, measured with a thermocouple on the precise location at which the probe is immersed in the liquid bath.

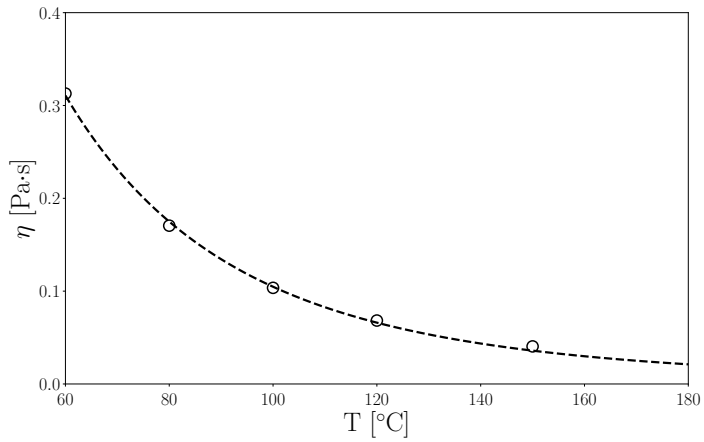

Figure II: Evolution of viscosity with temperature: comparison between the Arrhenius fit and the data yielded by the dependance on shear rate (empty circles).

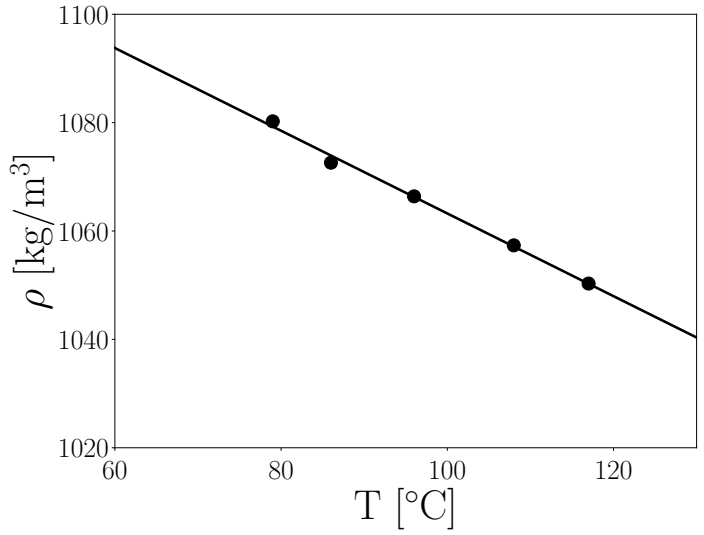

Figure III: Evolution of the density of PEG 3350 with temperature: experimental data and its corresponding linear fit.

Surface tension σ.

The surface tension was measured with a Krüss DSA100 drop shape analyzer, using the pendant drop method. Temperatures ranging from 80 to 120 °C with steps of 10 °C were explored, and each value was averaged over 10 droplets. The surface tension followed the Eötvös rule and could thus be fitted by a linear relation with respect to the temperature T in °C (Figure IV):

$$\sigma(T) = 47.14 - 0.08T \quad \text{mN/m} \tag{A.4}$$

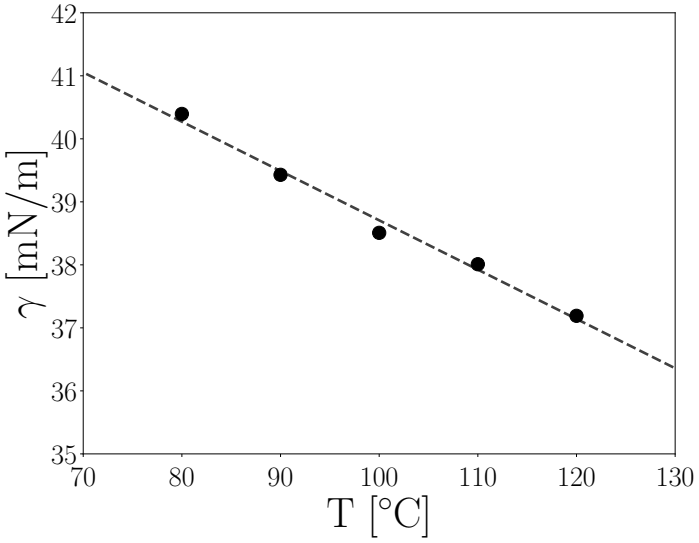

Figure IV: Evolution of the PEG 3350 surface tension with temperature: measurements and linear fit.

b. Substrates

The substrates used in this study were 23 µm thick NatureFlex™ NP cellulosic films provided by Innovia Films. They were bathed in ethanol for 1 h to remove the plasticizing glycerol on the surface, air-dried and cut with a scalpel to approximately $1\times2\,\text{cm}^2$ rectangles. The films presented oriented ridges when observed through a light source with the naked eye. They were cut so that the contact line would end up perpendicular to those ridges. The ridges were however not visible through a scanning electron or optical microscope. An earlier study on those same films [3] showed that they could be considered smooth compared to the scales at which the Cassie-Baxter and Wenzel models apply.

c. Dynamic contact angles

The dynamic contact angle formed by PEG on the cellulosic substrate was measured by the Wilhelmy method with a Dataphysics DCAT25 microbalance. The PEG was poured in the microbalance vessel and heated to 75 °C. A thermocouple was used to check the temperature at the center of the vessel.

The substrate was then attached to the microbalance, with the grooves perpendicular to the free surface. The vessel was moved upwards at a constant velocity V, until the substrate was plunged into the liquid with at immersion depth $h = 7\,\text{mm}$. At this point, the vessel was left to rest for 2 min (Figure V), and then lowered at the same velocity V.

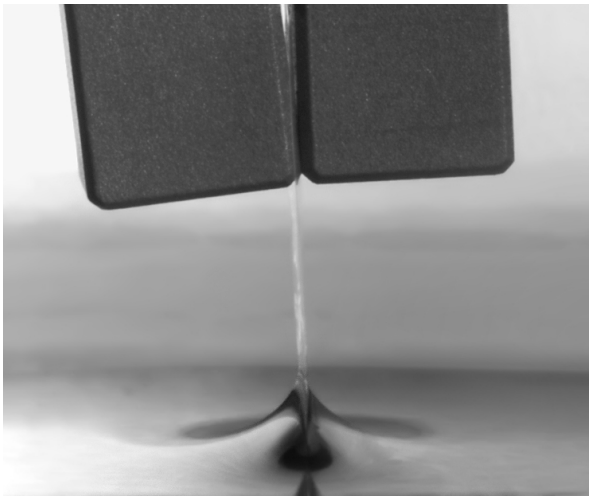

Figure V: Snapshot of the meniscus formed by PEG 3350 on a static cellulosic substrate, captured at an angle above the liquid surface. The substrate is attached to a microbalance, measuring the force exerted by the contact line. This allows to evaluate the macroscopic contact angle.

After detaching the substrate from the microbalance, its width w was measured carefully with an optical microscope to determine the length of the contact line $2w$. The thickness of the substrate was considered negligible.

The contact angle θ was then determined using the Wilhelmy equation, using a linear fit the on force - position relation to eliminate the effects of buoyancy and viscosity:

$$\cos\theta = \frac{F}{2\sigma w} \tag{A.5}$$

where F is the force exerted by the contact line, derived from the mass m yielded by the microbalance. The regression (Figure VI) enables the elimination of buoyancy and viscous drag on the substrate, assumed to be proportional to the depth of immersion h [2], by using the extrapolated value at the very beginning of immersion ($h = 0$).

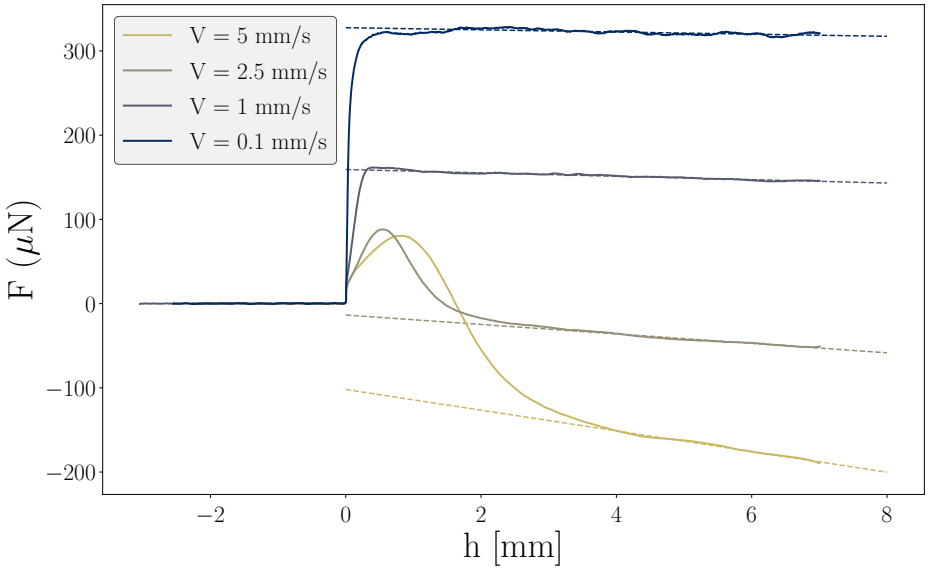

Figure VI: Tensiometric curves used to determine the dynamic contact angle for different velocities.

The equilibrium contact angle θ_e was determined using the last points of the resting phase, with the lowest velocities V used in this study. All of the low-velocity experiments yielded a similar value, so that this measurement was considered reliable. This was confirmed by further experiments, in which a substrate was immersed and the meniscus was left at rest, spreading for 5 h, yielding a value of θ_e within 1° of those measured by the previous method (Figure VII).

The dynamic contact angles of the advancing liquid were determined for a set of 8 different velocities. Velocities higher than $5\,\mathrm{mm \cdot s^{-1}}$ were not used: the corresponding menisci do not seem to reach a quasi-static equilibrium before approaching the bottom of the vessel. The dynamic contact angle θ versus capillary number Ca data was fitted with different models. Petrov and Petrov's model was deemed the most appropriate to interpolate the data (Figure VIII), and the resulting parameters are given in Table 2 for the PEG 3350.

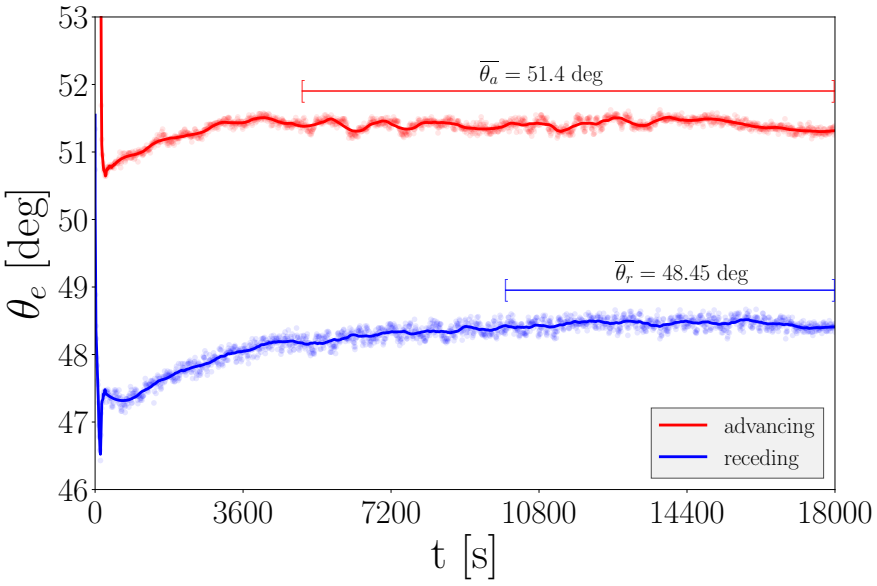

Figure VII: Static advancing and receding contact angles measured in a timespan of 5 h.

B. Numerical model

a. *Geometry*

The dimensions of the 2D domain were chosen to reproduce the experimental conditions. Considering the capillary length $\ell_c \approx 2\,\text{mm}$ in our experimental conditions, the domain requires a horizontal width L long enough so that far from the contact line, the interface stays unperturbed. Since the elevation of a meniscus decays exponentially as a function of the distance x to the surface of the plate [1], we will consider that it is at rest for $x > 5\ell_c$, and thus impose $L = 13\,\text{mm}$ to keep an extra margin for contact angle measurements. The symmetry boundary condition may then be used at the right-hand side of the geometry to obtain an unperturbed interface and flow.

The height of the domain H is also selected by considering the rise of a meniscus on a vertical plate. In a steady state, this height is $\ell_c\sqrt{2(1-\sin\theta_e)}$, which would amount to approximately 2.8 mm for total wetting in the present case. However, an advancing contact angle cannot be smaller than its equilibrium value, and our simulations deal with partially wetting liquids. With the equilibrium contact angles considered here, this height reduces

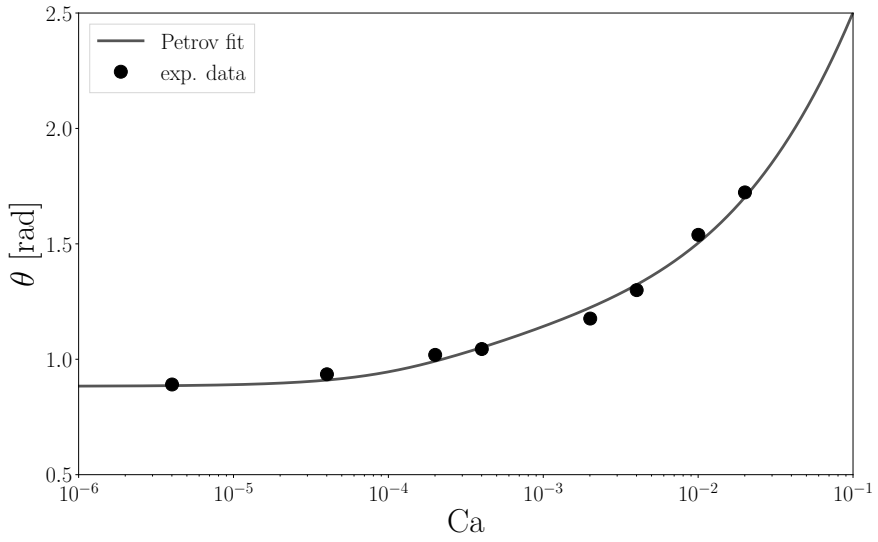

Figure VIII: Experimental measurements of dynamic contact angles formed by PEG 3350 on a cellulosic substrate, and their corresponding best Petrov-Petrov fit.

to less than 2 mm. Consequently, the domain height is chosen to be $H = 10\,\text{mm}$, to keep a safety margin like we did for the domain width, also allowing the flow to develop further from the interface.

b. Mesh, materials and parameters

The choice of an element size $h \leq 40\,\mu\text{m}$ was made by performing simulations on regular meshes of decreasing elements size, until reaching a stable macroscopic contact angle (Figure IX).

Since a refinement splits each element in two right triangles, with quadrangular initial elements, a convergence is reached after 4 iterations on the coarse mesh. The refinements are applied following the indicator $\sqrt{(\partial_x\Phi)^2 + (\partial_y\Phi)^2}/(x + L/4)$. This allows to increase the spatial resolution across the interface and around the contact line (Figure X), while keeping it coarser on the overall flow.

The characteristic interface width ε is set to be $h_0/2 = 80\,\mu\text{m}$. Initially, the reinitialization parameter γ_{LS} used in Equation 6 is chosen so that the mesh Péclet number $\text{Pe} = uh/(2\gamma_{LS}\varepsilon) = u/\gamma_{LS} = 1$. The maximum possible velocity is σ/η. But with this value

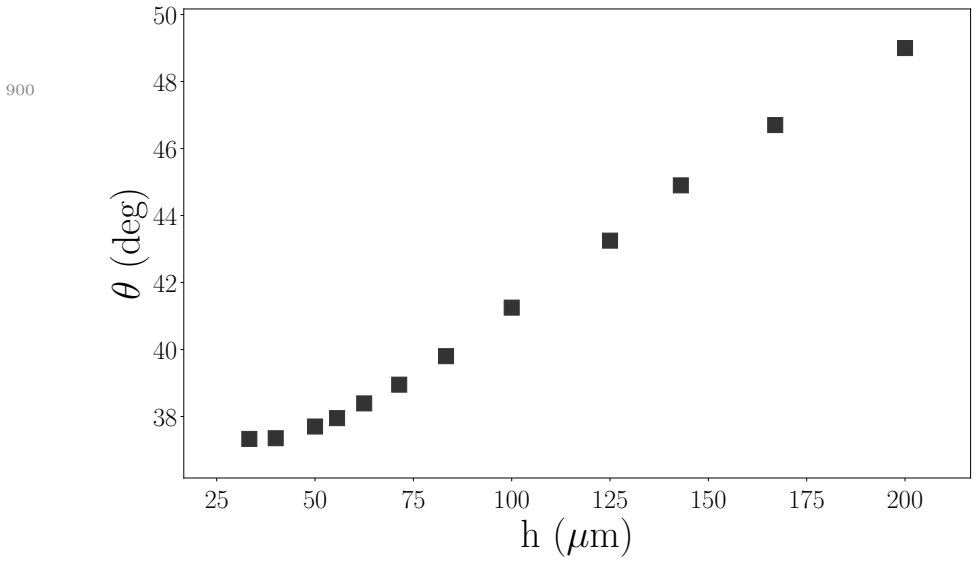

Figure IX: Mesh convergence study assessed by the evolution of the macroscopic contact angle as a function of element size h. A stable value is reached for $h \approx 40\,\mu\text{m}$.

the initial calculation conditions would be too severe and this would considerably lengthen the simulation time. A more reasonable value of $\gamma_{LS} = \sigma/(10\eta)$ was therefore chosen, which corresponds to a velocity associated with $\text{Ca} = 0.1$. This value is also a limit for the validity of the Cox model, and is thus seen as suitable. An insufficient rate of reinitialization is however known to cause the apparition of spurious currents. The set of parameters used here aims at avoiding them and usually succeeds. At large contact line velocities however, they sometimes become important. Unless noted otherwise, the sets of results displaying a noticeable amount of spurious currents are not presented or analyzed.

c. Slip profile

In Figure XI, the slip velocity inside the liquid $\Phi\, v_{slip}$ is plotted along the solid boundary for different plate velocities. Similarly to previous studies [4, 5], it appears that the GNBC produces a large slip in the vicinity of the contact line, and retains the same characteristics as those found by other authors.

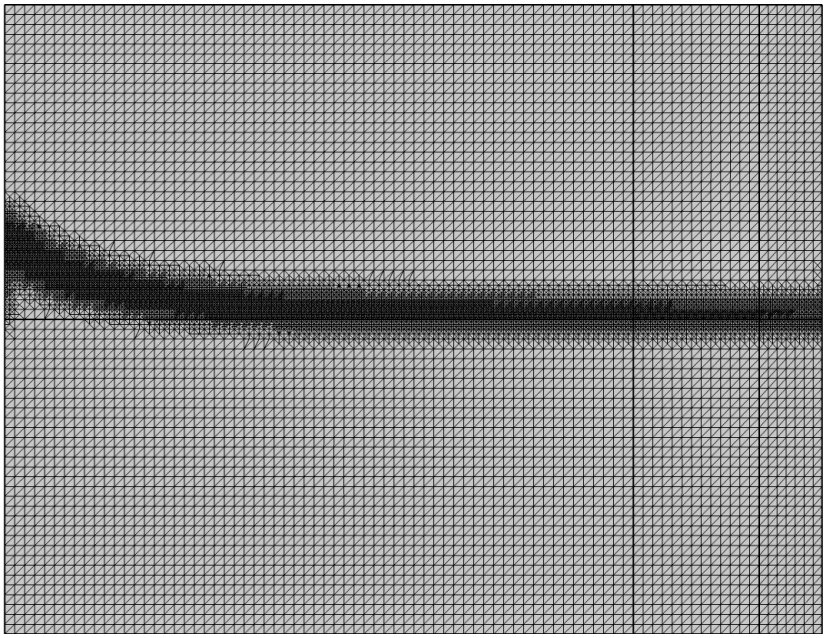

Figure X: Refined mesh obtained with a low plate velocity in a PEG 3350. The mesh displayed here contains 28563 elements, with sizes ranging from 40 to 160 µm. The PEG 3350 occupies the bottom part of the domain.

d. Preliminary results: contact angles

The macroscopic contact angles obtained for a constant slip length $\beta = h_0$ are compared to their experimental counterparts in Figure XII. The obvious discrepancy between numerical and experimental contact angles, along with the dependence of θ on β, lead to consider the use of a velocity-dependent slip length.

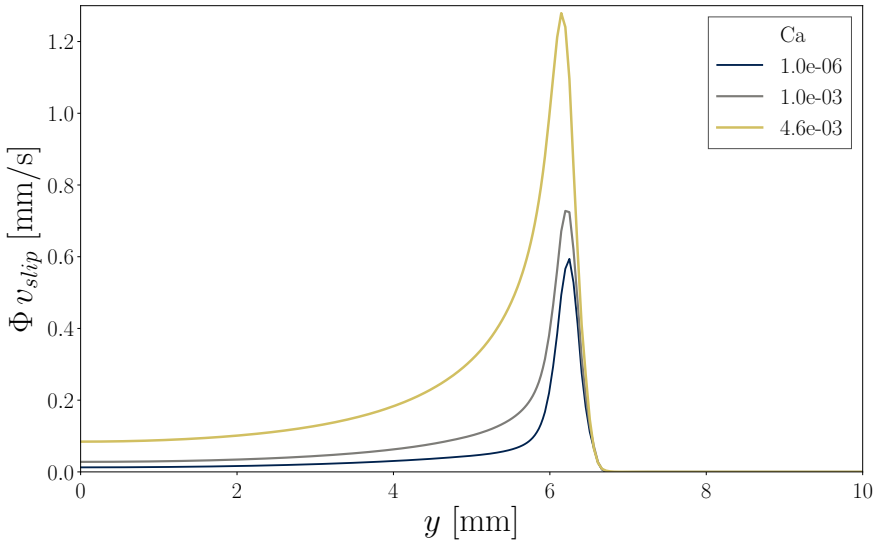

Figure XI: Slip velocity on the solid boundary for three different wall velocities. An important slip occurs across the contact line.

C. Influence of the slip length

a. Slip velocity and slip length

Estimations in the numerical simulations indicate an important difference between the slip velocity and the wall velocity (Figure XIII), especially at higher wall velocities. This means that the entrainment of liquid by the solid is losing efficiency as the velocity increases, and has a number of implications, such as interface shearing. It could also mean that the capillary number associated to high velocities is overestimated.

b. Dynamic wetting regime transition

The separation between microscopic and viscous dissipation can be controlled by the slip length, which sets the total dissipation. Here, we plot the difference between θ and θ_μ at various constant wall velocities, with relation to a continuously decreasing slip length (Figure XIV). The corresponding curves show the sudden separation between the main sources of dissipation.

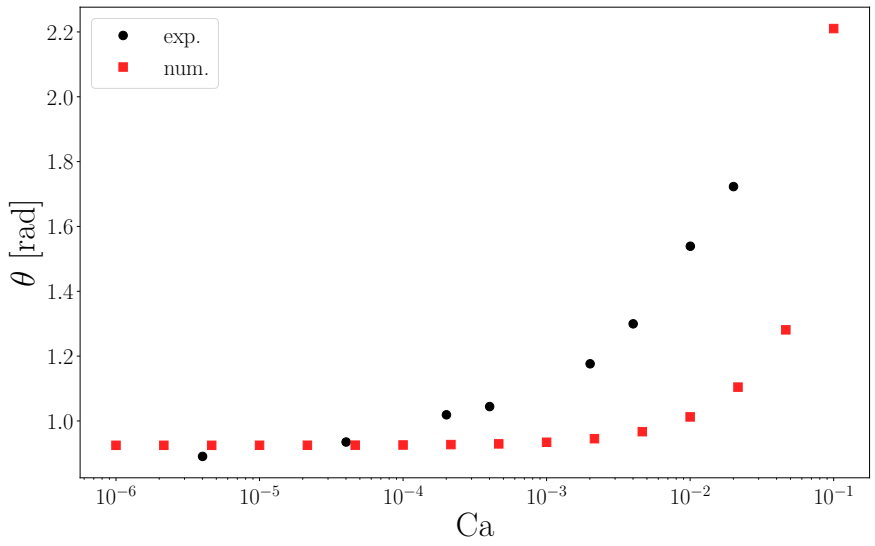

Figure XII: Dynamic macroscopic contact angle: comparison between the experimental values and the first numerical model ($\beta = h_0$).

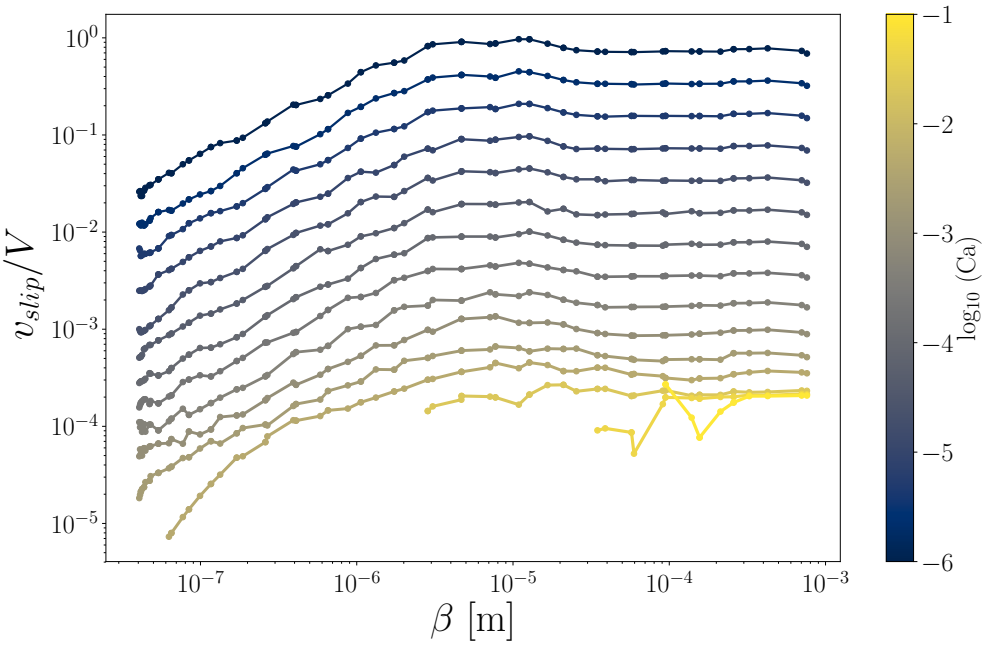

Figure XIII: Dependence of the relative slip velocity on the slip length.

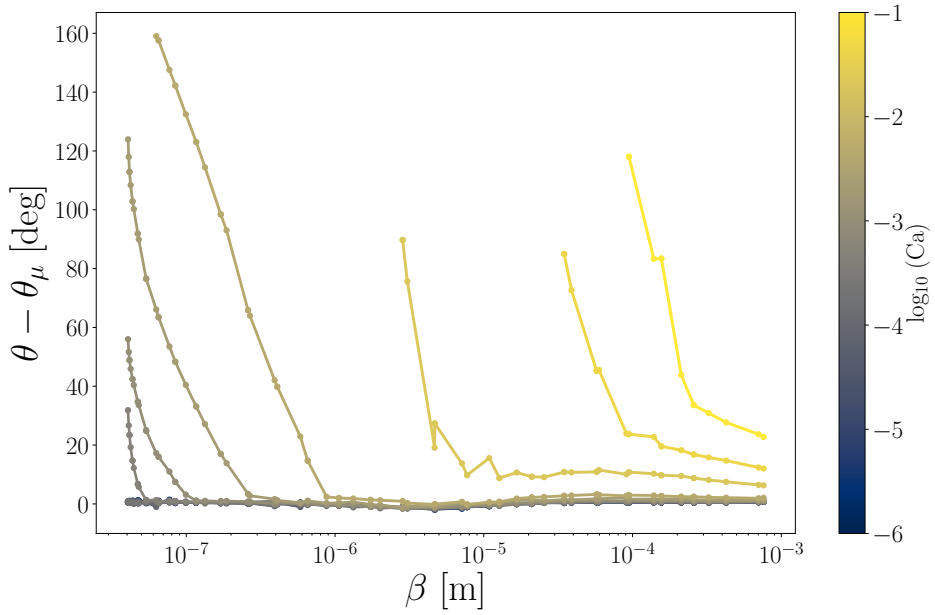

Figure XIV: Difference between the macroscopic and microscopic contact angle as a function of slip length, for different velocities.

References

[1] De Gennes, P.G., Brochard-Wyart, F., Quéré, D., 2015. Gouttes, Bulles, Perles et Ondes. Belin, Paris.

[2] Morra, M., Occhiello, E., Garbassi, F., 1992. The effects of velocity and viscosity on solid-liquid interfacial behavior during dynamic contact angle measurement. Journal of Adhesion Science and Technology 6, 653–665. doi:10.1163/156856192X01024.

[3] Pucci, M.F., Duchemin, B., Gomina, M., Bréard, J., 2018. Temperature effect on dynamic wetting of cellulosic substrates by molten polymers for composite processing. Composites Part A: Applied Science and Manufacturing 114, 307–315. doi:10.1016/j.compositesa.2018.08.031.

[4] Qian, T., Wang, X.P., Sheng, P., 2003. Generalized Navier Boundary Condition for the Moving Contact Line. Communications in Mathematical Sciences 1, 333–341.

[5] Ren, W., E, W., 2007. Boundary conditions for the moving contact line problem. Physics of Fluids 19, 022101. doi:10.1063/1.2646754.